Eidgenössische Technische Hochschule Zürich
Swiss Federal Institute of Technology Zurich

Eidgenössische Technische Hochschule Zürich
Fachbereich Physik

# Diploma thesis

## Quantum Electrodynamics with Superconducting Circuits: Measurement of the Cavity Photon Number using Ramsey Interference

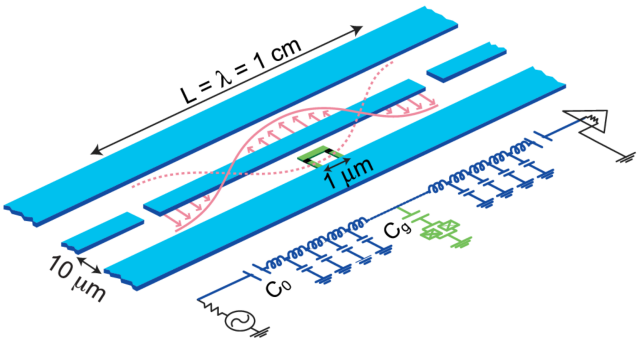


Presented by: Matthias Baur
Supervisor: Prof. Dr. Andreas Wallraff
Department: Solid State Physics

Zürich, August 2007

# Contents

# 1 Introduction

It all started at the beginning of the twentieth century when physics underwent a big revolution. Classical physics predicted several absurdities, like the ultraviolet catastrophe involving infinite energies of black body radiations, or electrons of an atom crashing into its nucleus only after a lifetime of $10^{-10}$ s, making the atoms extremely unstable. Max Plank solved the first problem in 1901 by assuming that the energies of harmonic oscillators inside a cavity is an integer multiple of some quantity (quantized). Built on this discovery, Albert Einstein proposed the quantization of electromagnetic radiation with the words:

> *"Monochromatic radiation with frequency $\nu$ of low density (inside the validity of the Wien distribution law) behaves in thermal theoretical relation, as if it consisted of each other independent energy quantums of value $h\nu$,"*

where $h$ is a new constant, the Planck constant. Light consists therefore, even though it has a wave like nature, of discrete energy packets called photons which Einstein used to explain the by then unexplained photo effect in 1905. This was the start of a new physics with a completely new type of thinking, the so called quantum theory. Even though many experts still find it very counterintuitive, it became one of the most successful theories, explaining the structure and stability of atoms, superconductivity, conductivity of metals and semi conductors, nuclear fusion in stars, just to mention a few.

As the understanding of quantum mechanics became better, clever scientists realized in 1970s-1980s that quantum mechanics could be used for information processing. The idea emerged when scientists were pondering the fundamental limits of classical computers. If technology continued to abide Moore's law stating that the number of transistors in a computer chip doubles every 18 month, then continually shrinking size of circuitry will reach a point where a single transistor reaches a size of a single atom. At those scales, classical physics brakes down and quantum mechanics becomes important. This gave rise to the question whether a new kind of computer could be developed on the principles of quantum mechanics. The first description of a universal quantum computer was provided by Davit Deutsch in 1985 [1] and it was shown later that a quantum computer can be significantly faster then a classical computer in specific cases. Peter Shor demonstrated 1994 an algorithm [2], that is able to factorize large numbers in seconds whereas a classical computer would take longer then the lifetime of our universe, and Lov Grover found in 1995 a search algorithm [3] faster then any classical counterpart, used to search entries in large databases. Another advantage of a quantum computer is the possibility to simulate quantum systems, which is not possible on a classical computer

in any efficient way as pointed out by Richard Feynman already in 1982 [4].

After these discoveries, intense search of suitable hardware to implement qubits has started. They are the smallest unit of information, consisting like the classical bit of two states 0 and 1, can however also possess a superposition state of those two. The physical implementation is a big experimental challenge, since the qubit should couple to the experimental setup strong enough that an experimenter can measure and control its state, should couple to its environment however as little as possible to prevent loss of information. One possible implementation is a superconducting electrical circuit acting as a qubit, called Cooper pair box (CPB). Coupling this circuit to a microwave cavity is one very promising approach to isolate the qubit from the environment outside the resonator while providing a good read out scheme at the same time [5]. Although microwaves do not have much in common with visible light, they are both electromagnetic fields and thus consist of photons. Coupling the qubit to those photons by applying microwave signals to the cavity, allow to measure and coherently control the qubit state or to measure the photons inside the cavity with the qubit.

The purpose of the diploma thesis presented here is the implementation of a phase gate by applying off resonant microwave pulses to the resonator. The accumulated relative phase in the qubit state induced by those microwave pulses due to the ac-Stark effect, can be measured using a Ramsey type interference measurement on the qubit state. From this experiment, the average photon number put into the cavity by those microwave pulses can be reconstructed. Understanding how the shape of those microwave pulses look like inside the resonator is essential to carry out this experiment and is thus analyzed carefully.

Chapter 2 reviews first the basics of qubits and shows the theory about the CPB and its coupling to a microwave resonator. This leads then to the discussion about cavity quantum electrodynamics (CQED) describing the coupling of the qubit with intra-cavity photons by the Jaynes-Cummings Hamiltonian and providing the measurement scheme used to determine the qubit state as well as the photon number inside the cavity. Chapter 3 shows the measurement setup used to perform our measurements. In chapter 4 several spectroscopic and time resolved measurements are shown. After that, the analysis of the resonator response to microwave pulses around its bare resonance frequency and their influence on the qubit state dephasing rate are shown. Those are all needed steps towards the implementation of the phase gate. The final implementation however couldn't be done because of a gate charge instability appeared in our qubit during the diploma thesis, which made it impossible to perform measurements on the qubit state.

# 2 Theory

At the beginning of this chapter the basics of quantum bits (qubits) and the theory of one possible physical implementation, the superconducting charge qubit is presented. Section 2 covers the theory of microwave cavities as a starting point for the discussion of the Jaynes-Cummings Hamiltonian (section 3) which describes the interaction between the qubit and the quantized electromagnetic modes inside a cavity. Such a system permits the read out of the qubit [5] as well as the photon numbers [6] inside the cavity. The scheme for such measurements is discussed at the end and used for later measurements.

## 2.1 Quantum bits

The smallest unit of information in a classical computer is the so called binary digit (bit) and has one of two possible values, 1 or 0. All information can then be constructed by combining consecutive bits into larger units. Like the classical bit, a quantum bit (qubit) can have two possible states $|0\rangle$ and $|1\rangle$. While the bit is either 0 or 1, the qubit can be in a linear superposition of both:

$$|\psi\rangle = \alpha\,|0\rangle + \beta\,|1\rangle\,, \qquad |\alpha|^2 + |\beta|^2 = 1, \tag{2.1}$$

where the numbers $\alpha$ and $\beta$ are both complex numbers.
Those qubit states life in a two dimensional Hilbert space $\mathcal{H}_2$ with the orthonormal basis $|0\rangle\,, |1\rangle$. Any quantum system that spans such a two dimensional Hilbert space can be used as a qubit. Also systems with multi dimensional Hilbert spaces could be used, if they possess two states that can be efficiently decoupled from the rest. There are several proposals for the physical implementation of a qubit, and several are successfully realized. Some important physical realizations of two level systems are:

- Cold ions trapped with electromagnetic fields, where the electronic states of the ion serve as the two level system [7].
- Polarization of single photons [8].
- Nuclear spins used in nuclear magnetic resonance (NMR) quantum computation [9], [10].
- Spin of electrons in single-electron quantum dots [11].
- Two level Rydberg atoms which are used in cavity quantum electrodynamics (CQED) quantum computation [12].

The system used in this diploma thesis is a Cooper pair box serving as a qubit that is coupled to an electromagnetic resonator, a superconducting solid state circuit. One major problem for building a quantum computer for solving complex problems, is scalability, the question of how to build a system with many qubits. The Cooper pair box is fabricated on a single micro-electronic chip which makes it in principle easy to develop scaled systems, has however the problem of decoherence, see 2.4, because a quantum system realized in solid state interacts strongly with the environment.

### Bloch sphere representation

In order to understand how a certain operation acts on a single qubit state, it is useful to have a visual picture of the dynamics. The Bloch sphere, see Fig. 2.1, is such a geometrical representation of a two dimensional Hilbert space. It is easy to see that a qubit state (2.1) can be rewritten as

$$|\psi\rangle = \cos\frac{\Theta}{2}|0\rangle + e^{i\phi}\sin\frac{\Theta}{2}|1\rangle\,, \tag{2.2}$$

where the global phase factor has been omitted since it is a non observable effect. The numbers $\Theta$ and $\phi$ define a point on a three dimensional unit sphere. Every vector to such a point on this sphere represents a qubit state, where vector to the north pole is defined as the ground state $|0\rangle$ and the vector to the south pole as the excited state $|1\rangle$. The processing of quantum information is done as in classical information with the help of elementary operations, so called gates. A quantum gate is a unitary operation on $\mathcal{H}_2$. Its action on a qubit state can be visualized as a rotation of the vector around some axis in the sphere.

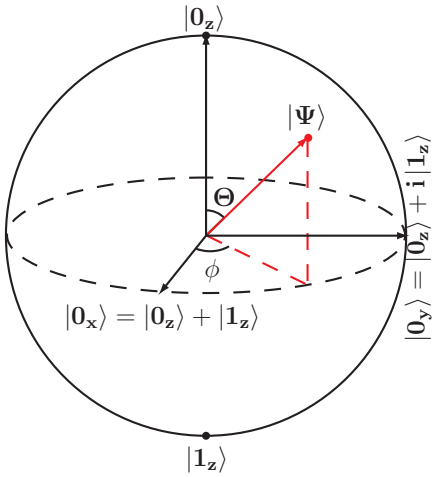


Fig. 2.1: Bloch sphere representation of a qubit state. Every single state of a two level system can be represented by a point on this sphere. The ground state is defined as the north pole, while the excited state is the south pole.

### 2.1.1 LC oscillator

The simplest electrical circuit that could be used as a qubit is the LC oscillator. It consists of two lumped elements, an inductor $L$ and a capacitor $C$, see Fig. 2.2(a). The Hamiltonian for this system can easily shown to be

$$H_{LC} = \frac{q^2}{2C} + \frac{\theta^2}{2L}, \tag{2.3}$$

where $q$ is the charge stored in the capacitor, and $\theta = LI$ the flux stored in the inductor. Those variables are the generalized canonical position and momentum variables. The quantization is done by simply replacing the classical variables by the quantum mechanical operators $(\hat{H},\ \hat{q},\ \hat{\theta})$ which satisfy the commutation relation $[\hat{q}, \hat{\theta}] = i\hbar$. One can then express the Hamiltonian in terms of dimensionless operators

$$H = \hbar\omega(a^\dagger a + \frac{1}{2}), \tag{2.4}$$

where the photon annihilation operator is given by

$$a = \frac{1}{\sqrt{2\hbar Z_c}}(\hat{\theta} + iZ_c\hat{q}), \tag{2.5}$$

where $Z_c = \sqrt{L/C}$ is the characteristic impedance of the circuit. In this language, the charge and flux can be expressed in terms of creation and annihilation operators as

$$\hat{q} = i\sqrt{\frac{\hbar}{2Z_c}}(a^\dagger - a), \tag{2.6}$$

$$\hat{\theta} = \sqrt{\frac{\hbar Z_c}{2}}(a + a^\dagger). \tag{2.7}$$

The energy levels of this system form a harmonic spectrum, shown in Fig. 2.2(b), where all the levels are equally separated from each other. In order to have a well isolated two level system however (for example the ground and first excited state), the transition energy between those two states must be sufficiently different from the transition to the next higher energy states. The only known dissipation free element that can be used to produce an anharmonic spectrum is the Josephson junction which has a strongly nonlinear dependence in the current flowing trough the junction.

### 2.1.2 Josephson junction

The Josephson effect is named after the British physicist Brian David Josephson who predicted 1962 the existence of the superconducting tunnelling effect of Cooper pairs [13]. We see the Josephson effect through a flow of electric tunnel current of Copper pairs between two superconducting materials that are separated by an extremely thin barrier. This arrangement is called a Josephson junction. Their properties are exploited not

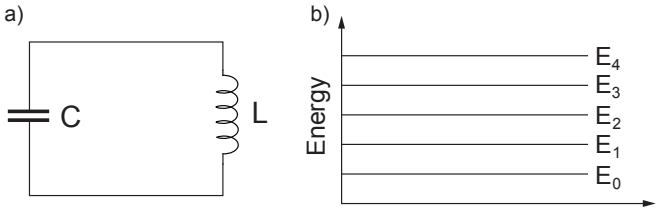


Fig. 2.2: **a)** Schematics of an LC oscillator consisting of two lumped elements $L$ and $C$. **b)** The harmonic spectrum of the LC oscillator.

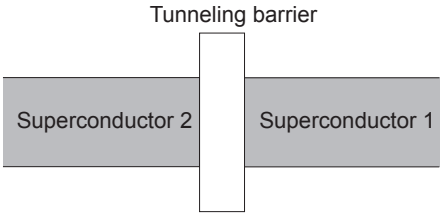


Fig. 2.3: Schematic image of a Josephson junction with two superconductors 1 and 2 and an insulator between them.

only for qubits but also in SQUIDs (Superconducting Quantum Interferometer Device) which allow measurement of tiny magnetic fields [14]. Even magnetic fields generated by electrical signals flowing between neurons in the brain can be detected.

For the theoretical description of the Josephson effect [15], we assume a simplified model as shown in Fig. 2.3. Two superconductor 1 and 2 are connected over a thin tunnel barrier. Assume the temperature is low, so that all electrons are in pairs in their common super conductive (BCS)-ground state, $\Delta/2$ under the Fermi energy. This state can be described in both superconductors by a macroscopic wave function whose square of amplitude is the local density of charge $\rho$:

$$\psi = \sqrt{\rho} e^{i\delta}, \tag{2.8}$$

where $\delta$ is an initially arbitrary phase. Let $\mathscr{H}_1$ and $\mathscr{H}_2$ be the Hamilton operators of each separated superconductor, we get for the coupled system over the barrier:

$$i\hbar \frac{\partial \psi_1}{\partial t} = \mathscr{H}_1 \psi_1 + T\psi_2, \tag{2.9}$$

$$i\hbar \frac{\partial \psi_2}{\partial t} = \mathscr{H}_2 \psi_2 + T\psi_1. \tag{2.10}$$

$T$ expresses the coupling constant which is characteristic for the tunnel barrier. The solution for this system of equations gives us the change $\dot{\rho}$ of the electron density, i.e.

for the electric current density, the nonlinear expression

$$i = i_0 \sin(\delta), \tag{2.11}$$

$$\delta(t) = \delta_0 + 2e/h \int_0^t V(\tau) d\tau, \tag{2.12}$$

where $i_0 = 2T\rho_0/\hbar$ is the critical current density of the junction, $\rho_0 = \rho_1 = \rho_2$, and $\delta = \delta_2 - \delta_2$ the phase difference of the wave functions. V is a potential difference between the superconductors.
Those results can be separated into two aspects of the Josephson effect:

**1. DC Josephson effect:** With no applied voltage across the insulator, the phase is constant and there may flow a direct current due to tunnelling.

$$V = 0 : \qquad i = i_0 \sin(\delta_0). \tag{2.13}$$

**2. AC Josephson effect:** With a fixed voltage $V_0$ applied across the junctions, the phase varies linearly in time and the current is a sinusoidal AC current at the Josephson-frequency $(2e/h)V_0$ with amplitude $i_0$

$$V \neq 0 : \qquad i = i_0 \sin(\delta_0 + 2\pi f_0 t), \tag{2.14}$$

$$\text{with } f_0 = (2e/h)V_0. \tag{2.15}$$

This nonlinear behavior of the current is used to create a superconducting circuit with a non harmonic energy spectrum. The theory for the simplest version, the Cooper pair box, is discussed in the next section.

### 2.1.3 Cooper pair box

The Cooper pair box was first discussed theoretically in 1987 by Büttiker [16] and experimentally realized by the Saclay group in 1997 [17]. Coherent quantum dynamics was first observed by the NEC group in 1999 [18].
The Cooper pair box (CPB) consists of a small superconducting island, which is connected to a Cooper pair reservoir over a Josephson junction with capacitance $C_j$, see Fig. 2.4. Single Cooper pairs can tunnel coherently from the reservoir trough the junction to the island and vice versa. A gate voltage $V_g$ applied to the gate capacitance $C_g$ controls the amount of charge on the capacitor $n_g = C_g V_g/e$ which in turn changes the amount of excess Cooper pairs $N$ (number of Cooper pairs with respect to neutrality) or excess charge $n = 2N$ on the island.

### Charge basis

The number of excess Cooper pairs on the island may be represented by the so called number operator $\hat{N}$. Its eigenstates $|N\rangle$ satisfy the relation

$$\hat{N}\,|N\rangle = N\,|N\rangle\,, \qquad N \in \mathbb{Z}. \tag{2.16}$$

The set $\{|N\rangle\,, N \in \mathbb{Z}\}$ forms a complete basis for the states of the box. If we neglect the tunnelling for the moment, the Hamiltonian of this system can be written as

$$H_{el} = 4E_C(\hat{N} - n_g/2)^2, \tag{2.17}$$

where $E_C = e^2/2C_\Sigma$ is the electrostatic charging energy needed to add single electrons to the island and $C_\Sigma$ the total capacitance of the CPB. The term describing the coherent tunnelling in the $|N\rangle$ basis, which is the number of Cooper pairs on the island, writes:

$$H_J = \frac{E_J}{2}\sum_N(|N\rangle\langle N+1| + |N+1\rangle\langle N|), \tag{2.18}$$

where $E_J$ is the Josephson coupling energy. This Hamiltonian lets Cooper pairs hop on and off the island at a rate $E_J/\hbar$. The complete Hamiltonian of the whole system is the sum of the Josephson and of the electrostatic Hamiltonian:

$$H_{CPB} = H_{el} + H_J = 4E_C(\hat{N} - n_g/2)^2 + \frac{E_J}{2}\sum_N(|N\rangle\langle N+1| + |N+1\rangle\langle N|). \tag{2.19}$$

The energy eigenstates $|k\rangle$ and their associated energies $E_k$ can be calculated from the Schrödinger equation

$$H_{CPB}\,|k\rangle = E_k\,|k\rangle\,, \qquad k \in \mathbb{N}^0. \tag{2.20}$$

This equation can't be solved analytically because the charge basis is unbounded and discrete. The energy spectrum shown in Fig. 2.5 can either be derived numerically or by diagonalizing the Hamiltonian in the phase basis, see next paragraph. The dashed and dotted parabolae, energy levels of the electrostatic Hamiltonian (2.17), are just the energies of a capacitor with some fixed charge. They correspond to the states with well defined number of Cooper pairs (zero, one, two,...) on the island. At the crossing points of the two parabolae, the two charge states are energetically degenerate. The additional Josephson term couples the two charge states $|N\rangle$ and $|N+1\rangle$. The eigenstates are at the degenerate point no longer well defined charge states, but become symmetric and antisymmetric superpositions $1/\sqrt{2}(|N\rangle \pm |N+1\rangle)$ which leads to an avoided crossing. The energy difference $E_{\text{diff}}$ of the ground and excited state is given by the Josephson energy $E_{\text{diff}} = E_J$. This forms a periodic band structure where the higher excited states are well separated from the first excited state and can therefor be used as a good approximated two level system. The whole energy level structure is fully determined by the two energies $E_C$ and $E_J$. In the regime where the charging energy is much larger than

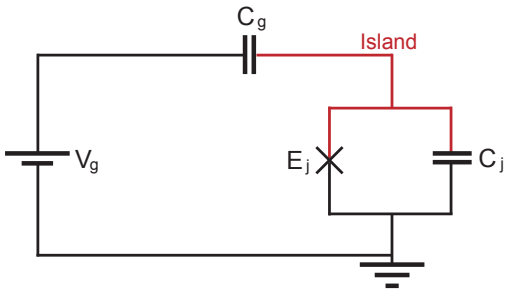


Fig. 2.4: Schematic of the Cooper pair box circuit. It consists of an island (red) connected to a reservoir over a Josephson junction which is shown here as a pure Josephson element and a capacitance $C_j$ from the contact in parallel.

the Josephson energy ($4E_C \gg E_J$), the charge qubit regime, fluctuations $n_g$ which arise from noise on the gate voltage and charges located in the dielectric around the qubit lead to fluctuations in the qubit transition energy. This is the main reason for dephasing of the qubit state, see also 2.4. At the degeneracy point $n_g$ however, often referred to as the sweet spot, it is in first order immune against those fluctuations and allows to reach longer coherence times [19]. In order to even make the qubit completely insensitive to charge noise, one can increase the ratio $E_J/E_C$ which flattens energy levels in charge axis. The transition frequency becomes completely insensitive to charge and therefor to charge noise. Qubits operated in this regime are called transmons [20] and is a major topic of current investigations.

Limiting ourself to the gate voltage between $0 < n_g < 2$, we can simplify things by considering only the two lowest energy levels $|0\rangle$ and $|1\rangle$. By choosing the zero energy to be $E_0 = 2E_C(1-n_g)^2$, the Hamiltonian can be written

$$H_{CPB} = -\frac{1}{2}E'_{el}\sigma_z - \frac{1}{2}E_J\sigma_x, \tag{2.21}$$

where $E'_{el} = 4E_C(1-n_g)$ and $\sigma_x$ and $\sigma_z$ are the Pauli matrices. One can identify this expression with a spin 1/2 particle in a magnetic field by rewriting this Hamiltonian to

$$H = -\vec{s}\cdot\vec{h}, \tag{2.22}$$

where $\vec{s}$ is the operator of the effective spin 1/2 and $\vec{h} = \vec{x}\cdot E_J/2 + \vec{z}\cdot[2E_C(1-n_g)]$ the magnetic field whose components are determined by the box parameters $E_c, E_J$. The energy eigenvalues are given by [21]

$$E_\pm = \pm\frac{1}{2}\sqrt{16E_C^2(1-n_g)^2 + E_J^2}, \tag{2.23}$$

with the corresponding symmetric and antisymmetric eigenstates up to the overall phase factor

$$\left|\psi_{s/a}\right\rangle = \cos(\frac{\phi}{2})\left|0\right\rangle \pm \sin(\frac{\phi}{2})\left|1\right\rangle, \tag{2.24}$$

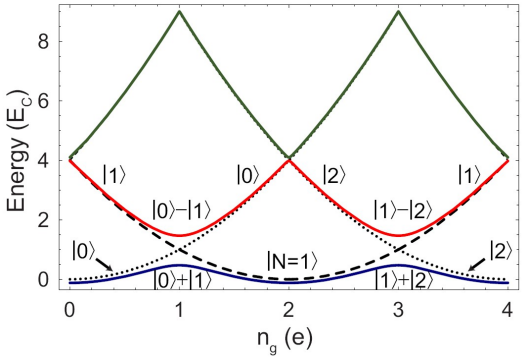


Fig. 2.5: CPB energy levels versus the charge $n_g$ induced by the gate voltage. Dashed and dotted lines show the electrostatic energy for 0,1 and 2 Cooper pairs on the island. The red, blue and green curves show the ground, and the first two excited state energy levels with $E_J = E_C$. At the degeneracy points ($n_g = 1, 3, 5, \ldots$) there is an avoided crossing of the energy parabolas where the eigenstates form a superposition of $N$ and $N+1$ Cooper pairs. Figure taken from [22].

where $\phi = \arctan\left(E_J/E'_{el}\right)$ is the mixing angle.

#### Phase basis

The conjugate variable of $\hat{N}$ is the superconducting phase $\hat{\delta}$ across the Josephson junction with eigenstates $|\delta\rangle$ such that

$$\hat{\delta}\,|\delta\rangle = \delta\,|\delta\rangle\,. \tag{2.25}$$

The set $\{|\delta\rangle\,,\ \delta \in [0, 2\pi]\}$ forms a complete basis of the box states. In this representation, the number operator becomes

$$\hat{N} = i\frac{\partial}{\partial\delta}. \tag{2.26}$$

The effect of the operators $\exp(i\hat{\delta})$ and $\exp(-i\hat{\delta})$ on the charge states is

$$e^{\pm i\hat{\delta}}\,|N\rangle = |N \pm 1\rangle\,. \tag{2.27}$$

The analytic eigenstates and their energies can be calculated by solving the Schrödinger equation corresponding to this Hamiltonian. This can be done with Mathieu functions, see [23] for details.

### 2.1.4 Split Cooper pair box

A big drawback of the previously discussed CPB is that the relevant parameters $E_C$ and $E_J$ are fully determined at the fabrication process. With the slightly improved

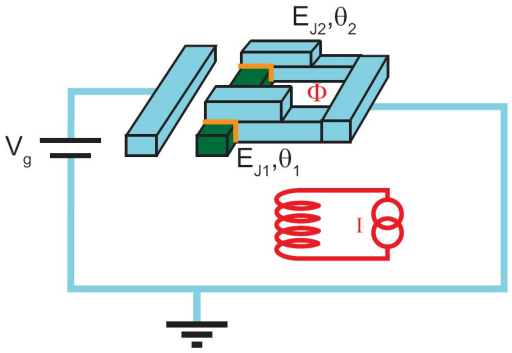


Fig. 2.6: Schematics of the split Cooper pair box. The island (green) is connected to the reservoir (blue) by two Josephson junctions, each with a Josephson energy $E_{J1}$,$E_{J2}$ and phase difference $\delta_1$,$\delta_2$. The effective $E_J$ can be tuned with a magnetic flux $\theta$ applied trough the loop. Figure taken from [22].

CPB shown in 2.6 which was used in our experiments, the whole energy spectrum can be controlled by tuning the Josephson energy and the gate Voltage. The Josephson junction is replaced by two that are joined to a segment of a superconducting ring and thereby form a superconducting quantum interference device (SQUID). A magnetic flux $\theta$ trough the loop controls $E_j$ that is given by[1]

$$E_J = (E_{J1} + E_{J2}) \cos(\pi\theta/\theta_0), \tag{2.28}$$

where $\theta_0 = h/2e$ is the superconducting flux quantum.

## 2.2 Microwave cavity

In circuit quantum electrodynamics (cQED) discussed in Sec. 2.3, the CPB is placed inside an electrical resonator which creates a standing wave that couples to the qubit. This system is used to read out the qubit state later. In this section, we first analyze a simple LRC oscillator which could act as a cavity. However, for microwave frequencies, it is not easy to work with true lumped element circuits because of the stray parameters becoming important at high frequencies. Thus, a 1D coplanar transmission line resonator is used and discussed, which can be modeled with a lumped LRC circuit.

[1]This expression is only exact when both Josephson energies are equal $E_{J1} = E_{J2}$

### 2.2.1 The LCR oscillator

The equation of motion for the amount of charge on the capacitor in a parallel LRC oscillator can be written as

$$\frac{d^2q}{dt^2} + \frac{1}{RC}\frac{dq}{dt} + \frac{q}{LC} = 0. \tag{2.29}$$

The solution to this differential equation is

$$q(t) = q_0 e^{i\omega_0 t - \frac{\kappa}{2}t + \phi} \tag{2.30}$$

which describes a charge oscillation with frequency $\omega_0 = 1/\sqrt{LC}$ and decay rate $\kappa = 2/(RC)$. In the frequency domain the circuit can be described by its impedance $Z(\omega)$ which can be written

$$Z_{LRC}(\omega) = \left(i\omega + \frac{1}{i\omega L} + \frac{1}{R}\right)^{-1}. \tag{2.31}$$

Near resonance, this expression can be expanded to first order in $\delta\omega = \omega - \omega_0$ leading to [24]

$$Z_{RLC}(\omega) = \frac{R}{1 + 2iQ\delta\omega/\omega_0} \tag{2.32}$$

where the quality factor of the resonator is $Q = \omega_0 RC = \omega_0/\kappa$. The quality factor is a dimensionless parameter that indicates the rate of energy dissipation relative to the oscillation frequency.

### 2.2.2 Transmission line

A good reference for the theory of transmission lines are chapters 2 and 3 from [24]. They can be schematically represented as a two-wire line (Fig. 2.7(a)), because transmission lines for TEM wave propagation (which is used in our setup) always have at least two conductors. One can model the transmission line as series of infinitesimally small circuits of lumped elements that has the same impedance per unit length as the transmission line, see Fig. 2.7(b), where the different elements are given by

- the series resistance per unit length $R^*$ for both conductors in $\Omega/m$ representing the resistance due to the finite conductivity of the conductors,
- the series inductance per unit length $L^*$ for both conductors in $H/m$ representing the total self/inductance of the two conductors,
- the shunt conductance per unit length $G^*$ in $S/m$ due to dielectric loss in the material between the conductors,
- the shunt capacitance per unit length $C^*$ in $F/m$ due to the close proximity of the two conductors.

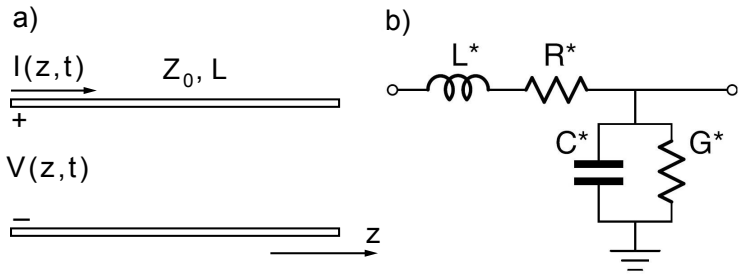


Fig. 2.7: **a)** Schematics of a transmission line with impedance $Z_0$. **b)** Lumped element model of an infinitesimally small segment of the transmission line with same impedance per unit length.

The characteristic impedance of an infinitely long lossy transmission line is

$$Z_0 = \sqrt{\frac{R^* + i\omega L^*}{G^* + i\omega C^*}}, \tag{2.33}$$

and can be reduced in a lossless case to $Z_0 = \sqrt{L^*/C^*}$. A signal propagates through the transmission line as a wave $e^{\gamma z}$ with the complex propagation constant $\gamma = \alpha + i\beta = \sqrt{(R^* + i\omega L^*)(G^* + i\omega C^*)}$. The imaginary part of the propagation constant ($\beta = \mathrm{Im}[\gamma]$) describes the phase of the wave and the loss is given by the real part ($\alpha = \mathrm{Re}[\gamma]$) which is called the attenuation constant. Let's now consider a transmission line with one open end. The impedance at the end is then (at least in the ideal situation) infinite and differs strongly from the characteristic impedance $Z_0$, which causes the wave reflecting back at the end. While the power flow for such a line is constant, the voltage $V$ (blue) and current amplitudes $I$ (red) oscillate with the position on the line, see Fig. 2.8(a). The impedance seen looking into the line varies therefor with position, see Fig. 2.8(b), and is given at distance $l = -x$ by

$$Z_{\mathrm{in}}^{\mathrm{open}} = -iZ_0 \coth(\gamma l). \tag{2.34}$$

For a transmission line with open ends on both sides, two different resonance types exist. Whenever the length of the line is an integer multiple of a half wavelength ($l = n\lambda/2 = \pi\nu/\omega_0$), there will be high impedance resonance. Whenever the length is odd multiple of a quarter wavelength ($l = (2n+1)\lambda/4$), there will be high admittance resonance. In our setup used in this diploma thesis, the $\lambda$ high impedance resonance has been used for which the resonance frequency is

$$\omega_{0,n}^{\mathrm{open}} = \frac{1}{\sqrt{L^*C^*}} \frac{n\pi}{l}. \tag{2.35}$$

The input impedance of such an open ended lossy transmission line (LTL) of length $l = n\lambda/2$ is given by

$$Z_{\mathrm{in}}^{\mathrm{LTL}} = Z_0 \coth(\alpha l + i\beta l), \tag{2.36}$$

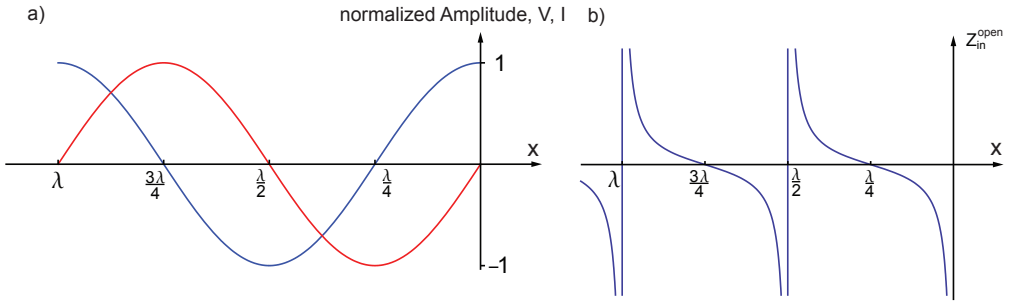


Fig. 2.8: **a)** The amplitude of the voltage $V$ (blue) and the current $I$ (red) oscillate with the length of a transmission line that is open on one end. **b)** The impedance $Z_{in}^{open}$ as a function of the position on the open transmission line.

which can be approximated around $\omega_0$ and for small losses $\alpha$ as

$$Z_{\text{in}}^{\text{LTL}} = \frac{Z_0}{\alpha l + i\pi \dfrac{\omega - \omega_0}{\omega_0}}. \tag{2.37}$$

The similarity of the two equations (2.32) and (2.37) allows one to map the one model to the other at the resonance $\omega_0$ with the substitution

$$R = \frac{Z_0}{\alpha l}, \tag{2.38}$$

$$C = \frac{\pi}{2\omega_0 Z_0}, \tag{2.39}$$

$$L = \frac{1}{\omega_0^2 C} = \frac{2Z_0}{\pi\omega_0}. \tag{2.40}$$

The quality factor Q of the transmission line can then be written as

$$Q = \omega_0 RC = \frac{\pi}{2\alpha l} = \frac{\beta}{2\alpha}. \tag{2.41}$$

### 2.2.3 Capacitively coupled transmission line resonator

So far we have discussed a transmission line resonator without any coupling to the environment. In order to be able to drive this resonator and measure the transmitted signal, one needs to connect an input and output transmission line. This is done in our setup via a small capacitor (see Fig. 2.9) that produces a large impedance mismatch and can be thought of as a "mirror", reflecting most of the incident radiation back but transmits a small amount. The effective shunt conductance $G_{\text{ex}}$ on resonance is given

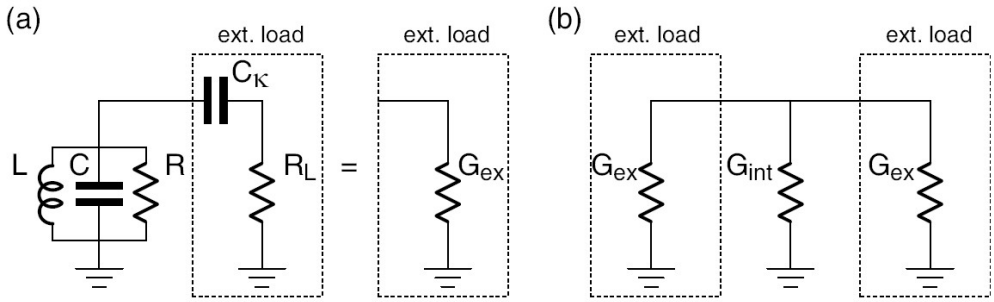


Fig. 2.9: **a)** LCR resonator coupled by a capacitor $C_k$ to load $R_L$. **b)** Resonator coupled to input and output lines.

by the real part of the impedance seen by the resonator at the coupling port and can be calculated with the Norton theorem

$$G_{ex} = Re\left(\frac{i\omega_n C_k}{1 + i\omega_n C_k R_L}\right) = \frac{R_L C_k^2 \omega_n^2}{1 + R_L^2 C_k^2 \omega_n^2}. \tag{2.42}$$

The external quality factor can then be defined as

$$Q_{ex} = \frac{\omega_n C_n}{G_{ex}}, \tag{2.43}$$

where $C_n$ is the capacitance defined in Eq. (2.39). When the resonator is symmetrically coupled to the input and output lines, this expression becomes $Q_{ex} = \omega_n C_n / 2G_{ex}$ and can be rewritten to

$$Q_{ex} = \frac{n\pi}{4Z_0}\left(\frac{1}{C_k^2 R_L \omega_n^2} + R_L\right). \tag{2.44}$$

The loaded quality factor $Q_L$ of the resonator can be found considering the parallel connection of the internal shunt $G_{int}$ and the external shunts $G_{ex}$

$$\frac{1}{Q_L} = \frac{1}{Q_{int}} + \frac{1}{Q_{ex}}, \tag{2.45}$$

with $Q_{int} = \omega_n C_n / G_{int}$. This gives some insights on how coupling to the environment gives an effective loss, and how that can be influenced during the engineering process.

### 2.2.4 Coplanar waveguide resonator

So far we have studied transmission line resonators without looking on the physical realization of the transmission lines. There are several possibilities such as microstrips, striplines and coplanar waveguides (CPW) which was used in our setup. It is composed of a median metallic strip separated by two narrow gaps from the ground planes forming

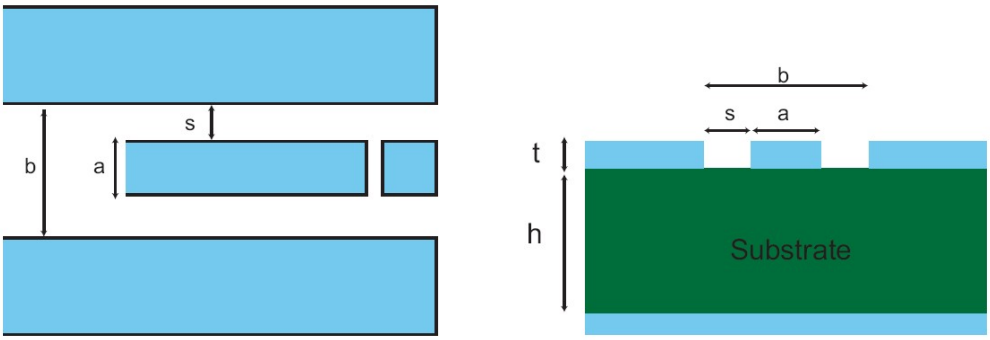


Fig. 2.10: Schematics of a coplanar waveguide. It consists of a median metallic strip line that is separated by two narrow gaps from the ground planes. The ratio $s/a$ determines the impedance $Z_0$. Figure taken from [22]

a 2d version of a coaxial cable, as shown in Fig. 2.10. The gaps can be scaled from some microns up to millimeters while leaving the impedance constant by varying the width of the central strip. The impedance is determined by the ratio $s/a$ and is given by [25]

$$Z_0^{CPW} = \frac{60\pi}{\sqrt{\epsilon_{eff}}} \frac{1}{\frac{K(k)}{K(k')} + \frac{K(k_3)}{K(k_3')}} \tag{2.46}$$

with the effective dielectric constant

$$\epsilon_{eff} = \frac{1 + \epsilon_r \tilde{K}}{1 + \tilde{K}}, \tag{2.47}$$

where K is the complete elliptic integral of the first kind and

$$\tilde{K} = \frac{K(k')K(k_3)}{K(k)K(k_3')}, \tag{2.48}$$

$$k = \frac{a}{b}, \tag{2.49}$$

$$k_3 = \frac{\tanh(\frac{\pi a}{2h})}{\tanh(\frac{\pi b}{2h})}, \tag{2.50}$$

$$k' = \sqrt{1-k^2}, \tag{2.51}$$

$$k_3' = \sqrt{1-k_3^2}. \tag{2.52}$$

$\epsilon_r$ is the relative dielectric constant of the substrate of height h.

## 2.3 Cavity quantum electrodynamics

Cavity quantum electrodynamics (CQED) studies the properties of atoms coupled via an electric dipole to discrete photon modes in cavities. These systems have the advantage of the possibility to reach high coupling strength even with just one photon, since the photon is bouncing back and force inside the cavity, giving it a lot of chances to interact with the atom, see Fig. 2.11(a). This coherent dynamics of the system is described by the Jaynes-Cummings Hamiltonian [26]

$$H_{JC} = \hbar\omega_r(a^\dagger a + 1/2) + \hbar\frac{\omega_a}{2}\sigma_z + \hbar g(a^\dagger\sigma^- + a\sigma^+), \tag{2.53}$$

where

| | |
|---|---|
| $\sigma_z = (\|1\rangle\langle 1\| - \|0\rangle\langle 0\|)$ | Pauli z-operator with $\|0\rangle$ and $\|1\rangle$ referring to the ground and excited state of the atom, |
| $\sigma^- = \|0\rangle\langle 1\|$ | Atomic lowering operator describing the transition from excited to ground state, |
| $\sigma^+ = \|1\rangle\langle 0\|$ | Atomic raising operator describing the transition from ground to excited state. |

The first term describes the energy of the electromagnetic field, where each photon contains an energy quantum $\hbar\omega_r$. The second term represents the atom as a spin 1/2 particle, with transition energy $\hbar\omega_a$ and can also be referred to as our CPB as we have seen in Section 2.1.3. The third term describes the dipole interaction where the atom can absorb ($\sigma^+ a$) and emit ($a^\dagger\sigma^-$) a photon from/to the field at rate g. Additionally to the coherent part, decoherence effects have to be taken into account such as the coupling of the cavity to the continuum which produces the cavity decay rate $\kappa = \omega_r/Q$ and the coupling of the atom to modes other than the cavity mode which cause the excited state to decay at rate $\gamma_1$. When the transition frequency $\omega_a$ of the atom and the resonance frequency $\omega_r$ of the cavity is the same (detuning $\Delta = \omega_r - \omega_a = 0$), the photon number state $|n\rangle$ and the atom ground and excited states $|\uparrow\rangle$,$|\downarrow\rangle$ are no longer eigenstates of the full Hamiltonian (2.53). They get split by the interaction term into a symmetric and an antisymmetric superposition of atom state and cavity state $|\Psi_\pm\rangle = (|\uparrow\rangle|n+1\rangle \pm |\downarrow\rangle|n\rangle)/\sqrt{2}$, which splits the energy levels by $2g\hbar\sqrt{n+1}$, see Fig. 2.11(b). This describes a maximally entangled state between the cavity mode and the atomic state. An initial state with an excited atom and zero photons $|\downarrow\rangle|0\rangle$ will therefore flop into the atomic ground state and one photon inside the cavity $|\uparrow\rangle|1\rangle$ and back again. This process is the so called Rabi oscillation at the vacuum Rabi frequency $g/\pi$. Systems that allow to perform several Rabi oscillations before the photon decays ($g \gg \kappa, \gamma_1$) are called to be in the strong coupling limit, which can be reached with high-Q cavities to reduce the decay times and large fields inside the cavity to achieve high coupling strength.

### 2.3.1 Dispersive limit

In the dispersive limit where the detuning is large enough ($g/\Delta \ll 1$), direct atomic transitions do not occur but nevertheless dispersive interactions between a single atom and a cavity field do occur. The Hamiltonian in this regime can be derived with second order time dependent perturbation theory of the Jaynes-Cummings Hamiltonian Eq. (2.53) and expanding the terms into powers of $g/\Delta$, yielding [27]

$$H \approx \hbar \left(\omega_r + \frac{g^2}{\Delta}\sigma_z\right)\left(a^\dagger a + \frac{1}{2}\right) + \frac{\hbar\omega_a}{2}\sigma_z. \tag{2.54}$$

The interaction through the dispersive shift term proportional to $g^2/\Delta$, shifts the energies of both the atom and the photons, see Fig. 2.11(c). The first term is similar to the Hamiltonian of a harmonic oscillator (Eq. (2.4)), with the oscillation frequency $\omega_r' = \omega_r \pm g^2/\Delta$ depending on the state of the atom. This allows us to perform a quantum non-demolition (QND) measurement to evaluate the state of the atom, see 2.3.3. To see the other effect of the dispersive interaction on the atom, the Hamiltonian can be rewritten as

$$H \approx \hbar\omega_r \left(a^\dagger a + \frac{1}{2}\right) + \frac{\hbar}{2}\left(\omega_a + \frac{2g^2}{\Delta}a^\dagger a + \frac{g^2}{\Delta}\right)\sigma_z. \tag{2.55}$$

It is easy to see in this writing, that the interaction increases the transition frequency of the atom by the photon number dependent ac-Stark shift $2g^2a^\dagger a/\Delta$ and the constant Lamb shift $g^2/\Delta$. This ac-Stark effect can be used to implement a phase gate and to perform a QND measurement on the photon number inside the cavity, which is the topic of this diploma thesis and discussed in section Sec. 4.3. It is important to see that neither the state of the atom nor the photon state is being destroyed in both cases!

### 2.3.2 Coupling CPB to cavity

To achieve the previously discussed system with our artificial atom (CPB), the configuration in Fig. 2.12 has been used. The CPB is placed in the center of the electrical CPW resonator, where the electric field component of the standing wave of the first harmonic is largest, in the space between the center conductor and the ground planes of the resonator. The island lies in parallel to the center conductor with a small gap in between. This allows us to apply a DC voltage to the center conductor of the resonator via capacitive coupling over the input gap capacitance and therefore apply a gate voltage $V_{DC}$ to the CPB over the gate capacitance between the center conductor and the island. The total voltage between the center pin and the ground is the sum of $V_g$ and the AC quantum voltage $V$ due to the photons present inside the cavity

$$V_g = V_{DC} + \hat{V}, \tag{2.56}$$

where $\hat{V} = \hat{q}/C$. This can be written with (2.6) as

$$\hat{V} = \sqrt{\frac{\hbar\omega_r}{2C}}(a + a^\dagger) = V_0(a + a^\dagger), \tag{2.57}$$

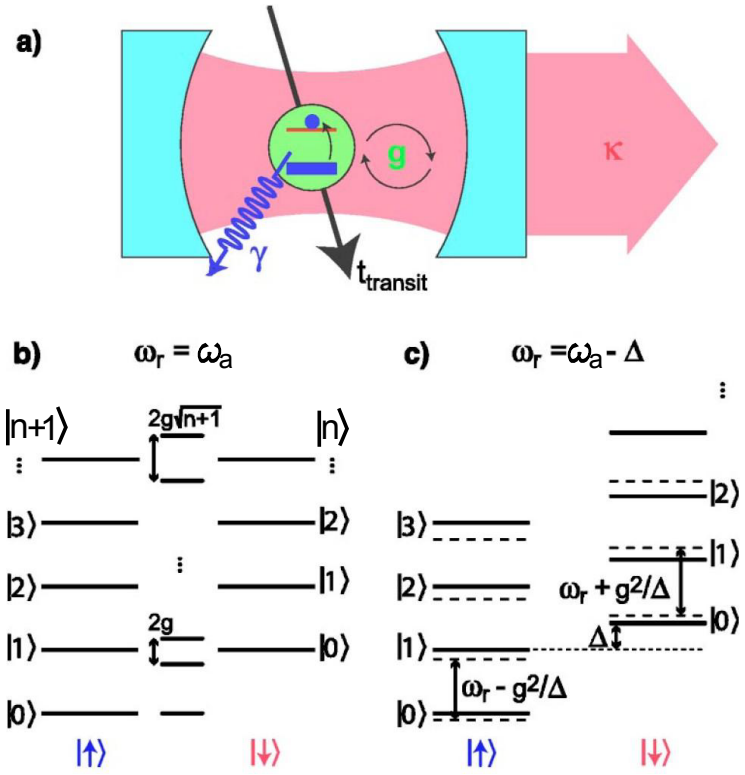


Fig. 2.11: **a)** Standard representation of a cavity quantum electrodynamic system. A two-level system with spontaneous decay rate $\gamma$ passes a cavity with decay rate $\kappa$. During the transit time $t_{transit}$, it couples to a single mode of the electromagnetic field confined between the two mirrors, where the coupling strength is $g = E_{rms}d/\hbar$. The energy spectrum of the coherent Jaynes-Cummings Hamiltonian is shown in b) and c). The dashed lines are the eigenstates of the uncoupled Hamiltonian, where left is the atom in the ground state $|\uparrow\rangle$, right in the excited state $|\downarrow\rangle$ and $|n\rangle$ corresponds to the photon number. **b)** In the case for zero detuning ($\Delta = 0$), the degeneracy gets split by a value $2g\sqrt{n+1}$ proportional to the coupling strength. **c)** In the dispersive limit, the levels get lifted by an amount $\pm\frac{g^2}{\Delta}$ independent of the photon number n, but dependent on the state of the atom(- for ground state, + for excited state). This figure was adapted from [28].

with $V_0$ being the rms vacuum voltage fluctuation in the resonator. Plugging this into the electrostatic Hamiltonian of the CPB (Eq. (2.17)) and expanding the square gives

$$H_{el} = 4E_C\left(\hat{N} - n_g/2\right)^2 + \frac{4E_C C_g \hat{V}(C_g\hat{V}/e + n_g/4)}{e} - \frac{4E_C C_g \hat{V}\hat{N}}{e}. \tag{2.58}$$

The first term is the original electrostatic Hamiltonian with the DC voltage as bias ($n_g$ is still just the charge of $V_C$). The second term is the extra energy stored in the geometric capacitance of the qubit, and is not state dependent, hence does not effect the dynamics of the coupled qubit-cavity system and will be omitted in future. The final term represents the cavity-CPB coupling and depends on both the CPB state (with $\hat{N}$) and the quantum field state of the resonator ($\hat{V}$). The coupling Hamiltonian can therefore be written as

$$H_{\text{coup}} = 2\hbar g(a^\dagger + a)\hat{N}, \qquad g = \frac{C_g}{C_\Sigma}\frac{eV_0}{\hbar}. \tag{2.59}$$

The ratio $C_g/C_\Sigma$ is the gate capacitance divided by the total capacitance of the CPB and denotes the division of voltage in the CPB. The coupling strength $2\hbar g$ is therefore the energy needed to move a Cooper pair across the portion $C_g/C_\Sigma$ of the rms vacuum voltage fluctuations $V_0$ in the resonator.
Let us assume the CPB to be biased at the degeneracy point $n_g = 1$ where the number operator of the Cooper pairs on the island can be written as $\hat{N} = \sigma_x/2$. One can then make a rotating wave approximation of Eq. (2.59) which ignores fast oscillating terms $a^\dagger\sigma^+$ and $a\sigma^+$, yielding

$$H_{\text{coup}} = \hbar g(a^\dagger\sigma^- + a\sigma^+). \tag{2.60}$$

Adding this together with the Hamiltonian of the resonator and the CPB contribution one obtains the Jaynes-Cummings Hamiltonian Eq. (2.53).

### 2.3.3 Dispersive readout of the qubit state

The interaction of the photons in the cavity with the qubit in the dispersive regime can be used to measure the state of the qubit. As we have seen in Sec. 2.3.1, the effective resonance frequency of the cavity $\omega_r' = \omega_r \pm g^2/\Delta$ is dependent on the state of the qubit, which means that the qubit state is mapped onto the effective resonance frequency of the cavity. The most sensible way to measure $\omega_r'$ is to irradiate a microwave field on the bare resonance frequency and then probe the phase difference of the transmitted signal with respect to the input signal, see Fig. 2.13. This phase shift can be evaluated to be $\delta\Phi = \arctan[2g^2/(\kappa\Delta)]$. For the qubit in the excited resp. in the ground state, the phase is maximally $\pm 90°$ deg, for a superposition $(1/\sqrt{2}\,|0\rangle + 1/\sqrt{2}\,|1\rangle)$ it is 0. For measurements, where all states between $|0\rangle$ and $|1\rangle$ should be resolved, this method works fine as long as the line width of the transmission spectrum is in the order of the dispersive resonance frequency shift $g^2/\Delta \approx \kappa$, where the slope of the phase curve is high enough to resolve all states $(\alpha\,|0\rangle + \beta\,|1\rangle)$. If one is only interested in either the ground or excited state, the best limit to work with is $g^2/\Delta \gg \kappa$.

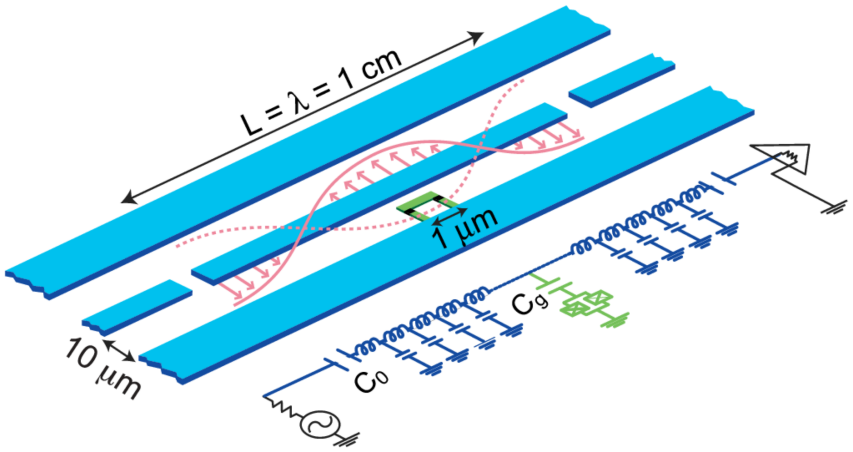


Fig. 2.12: Schematic layout of the cavity QED circuit with the equivalent lumped circuit representation. It consists of the 2D coplanar transmission line resonator, with the CPB placed in between the center pin and a ground plane where the standing wave has its maximum value, and is capacitively coupled to the center pin. This yields to a strong electric dipole interaction between the qubit and a single photon inside the cavity. Figure is taken from [28].

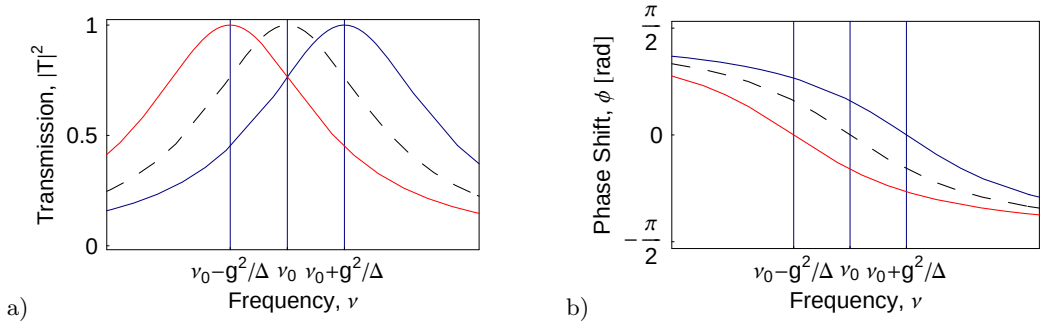


Fig. 2.13: Amplitude **a)** and phase **b)** of the transmission spectrum of the cavity for different qubit states. The black dashed curve represents the cavity without the presence of the CPB, while the red resp. blue curves correspond to the ground resp. to the excited state. The qubit state can be determined by either measuring the amplitude or the phase of a transmitted microwave signal at the bare resonance frequency of the cavity. Figure is taken from [29]

## 2.4 Decoherence in a Cooper pair box

The quantum coherence of the Cooper pair box is limited by its interaction with the degrees of freedom of its environment which leads to complex entanglement between them, including the measuring circuit [30], [31]. There are three types of decoherence, dephasing, energy relaxation and excitation of the box state, see Fig. 2.14. Dephasing processes randomly modify the relative phase of the two qubit states $|0\rangle$ and $|1\rangle$ leading to a state whose relative phase is completely unknown, whereas energy relaxation and excitation describe upward respectively downward transition of the qubit state.

The environment includes different type of degrees of freedom. Randomly moving charges in the insulting material close to the island, as well as single electron tunneling through the Josephson junctions mainly induce dephasing because they randomly vary the transition frequency of the qubit. Moving magnetic vortices in the super conductors and noise in the magnetic field lines could also play a role in the dephasing. Photons produced by the measuring process induce dephasing (see Sec. 4.3.2), relaxation and excitation. There are many more reasons for decoherence in the CPB, see [22] for more details.

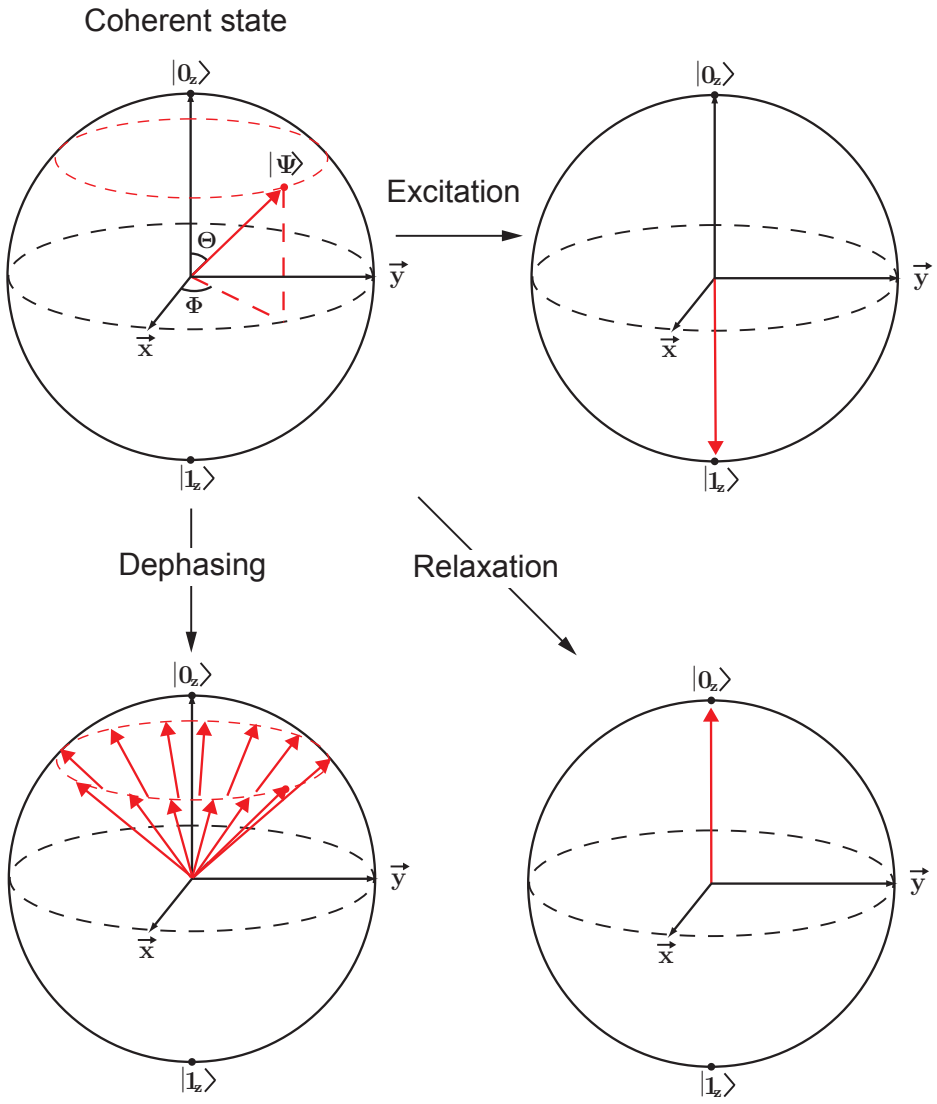


Fig. 2.14: A coherent state of a two level system (top left) coupled to its environment undergoes three different types of decoherence. In the rotating frame, dephasing corresponds to a diffusion of the state vector around the z-axis (bottom left). Relaxation corresponds to transition into state $|0\rangle$ (bottom right) while excitation describes a transition to state $|1\rangle$ (top right).

# 3 Measurement setup

As discussed earlier, the qubit state is probed by measuring the transmission of a microwave signal through the cavity and controlled by microwave pulses applied to the cavity. In order to perform those measurements, an appropriate measurement setup has to be used whose components are listed in the following and discussed individually in the next sections:

- The sample consists of the CPB coupled to a resonator.
- Phase coherent microwave sources with fast amplitude modulation for the measurement and coherent control of the qubit and DC sources for the gate voltage and the magnetic field (top left section in Fig. 3.2).
- Dilution refrigerator to reach base temperatures around 20 mK (second main block in Fig. 3.2).
- Cabling with low loss, filtering and attenuation of the signal lines before they reach the sample.
- Low noise amplification on the way back from the sample to room temperature.
- Data acquisition (top right section in Fig. 3.2).

## 3.1 The sample

The sample we have used during this diploma thesis contains a Cooper pair box in the charge regime and was fabricated lithographically at Yale University in 2004 and already used for previous experiments [32]. The upper optical microscopy picture in Fig. 3.1 shows the whole sample with the resonator and the CPB in the middle, while the two lower ones show a zoomed in picture of a coupling capacitor and a scanning electron microscopy picture of the CPB.

**CPB:** The three important parameters of the CPB are the charging energy $E_C$, the Josephson energy $E_J$ and the coupling strength g. They can all be freely chosen during the fabrication process and can be tuned for individual needs. The material used was aluminum with a critical temperature of 1.2 Kelvin evaporated on silicon substrate.
For measurements at the sweet spot, the qubit transition frequency is mainly determined by the Josephson energy. It has to be much larger then the thermal energy $k_B T \approx 20\,\mathrm{mK}$, but not too high that the microwave engineering becomes too hard. Reasonable values

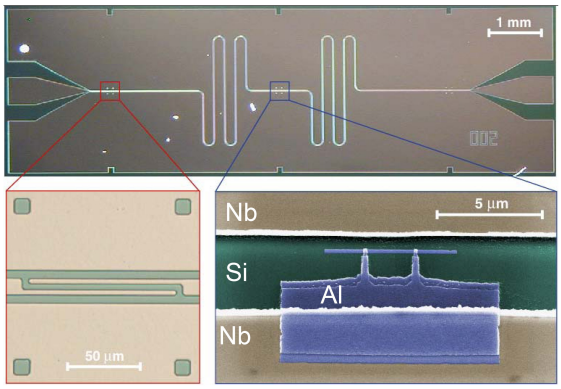


Fig. 3.1: Optical microscope image of the on chip resonator with the CPB placed in the middle. The left lower image shows a zoom in of one coupling capacitor. In the right lower edge, a false-colored SEM image of the CPB (aluminum blue) is shown, that is placed between the center pin and the ground plane of the niobium (beige) resonator on a silicon substrate (green). The two white points on the island are the Josephson junctions connecting the island with the reservoir.

would be $\sim 4\,\mathrm{GHz} - 8\,\mathrm{GHz}$ and $E_J$ turned out to be approximately 3.7 GHz for this sample. The coupling strength is approximately $g/2\pi = 20\,\mathrm{MHz}$.

**Cavity:** The important parameters are the resonance frequency controlled by the length and dielectric properties of the substrate, the quality factor determined by the size of the coupling capacitors and the impedance determined by the ratio of the center pin width to the size of the gap between the center pin and the ground planes. In order to reach resonance frequencies of 5.4 GHz used in this sample, the resonator length is realized in a meandering shape. It is fabricated with optical lithography technics on a silicon substrate and a metalization layer composed of niobium. The quality factors Q was around 6500.

## 3.2 Microwave signal synthesis

The measurement and control of the qubit is performed with microwave pulses. We use three microwave signal generators to produce classical phase coherent signals up to 20 GHz. The generation of the envelope pulses for the modulation is done with an arbitrary waveform generator, which has two analog outputs with 10 bit resolution and four digital outputs used as markers for the triggering of the microwave generators and acquisition card. The sampling rate of 1 Gs allows us to generate short pulses on nanosecond timescales. Pulse sequences with a maximum length of four million points are designed in Mathematica and loaded into the memory of the AWG. These envelope pulses are

then up converted to the microwave frequency by mixing them with an microwave tone. In order to do this phase sensitively, an IQ single-sideband up converter was used. This device has three inputs, the RF input, two intermediate frequency (IF) inputs I and Q (DC-500MHz) and one RF output. The RF input is split with a power divider into two signals. One of them is directly multiplied with the I input while the other is first phase shifted by -90 deg before being multiplied with the Q input. Those two branches are then combined again and output at the RF port.
To better understand the I and Q inputs, lets consider a signal $S(t) = A\cos(\omega t + \alpha)$. This can be rewritten with some trigonometry as

$$S(t) = A\cos(\alpha)\cos(\omega t) - A\sin(\alpha)\sin(\omega t) = I\cos(\omega t) - Q\sin(\omega t). \tag{3.1}$$

I is called the amplitude of the in-phase carrier and Q the amplitude of the quadrature phase carrier. We can therefore represent the state of the sine wave $S(t)$ by a vector in a complex plane with the real axis being I and the imaginary axis being Q. The amplitude is represented by the length of the vector $A$, while the phase is given by the polar angle $\alpha$

$$A = \sqrt{I^2 + Q^2}, \tag{3.2}$$
$$\alpha = \arctan(I/Q). \tag{3.3}$$

That means that we can adjust both the amplitude and the phase simply by changing the voltages applied to I and Q ports. One can for example apply a DC pulse on Q, which will cause the RF input signal being transmitted but with a phase shift of 90 degrees. If one applies pulses with a finite intermediate frequency $\omega_{IF}$, two sidebands[1] of frequency $\omega_{RF} \pm \omega_{IF}$ are transmitted. When both I/Q inputs are set to ground, no signal should be transmitted in the ideal case. In the reality however, there is still a small leakage signal present which could drive unwanted transitions of the qubit and add additional decoherence. In order to avoid this leakage, the signal generators are switched on an off with markers controlled by the AWG right before and after a pulse. Another marker is used to trigger the data acquisition.
All signal generators, the AWG and the data acquisition card are phase locked with a 10 MHz reference signal provided by a 10 MHz rubidium frequency standard. This is needed for phase sensitive controlling of the qubit state. With only the internal 10 MHz clocks was used rather then the frequency standard, noticeable phase shifts would occur during long acquisition times.

## 3.3 Cryogenics and filtering

In order to obtain long decoherence times, it is important to suppress quasi particle excitations in the superconductors. This demands a sample temperature way below the

[1] In our mixer one sideband is blocked by special design.

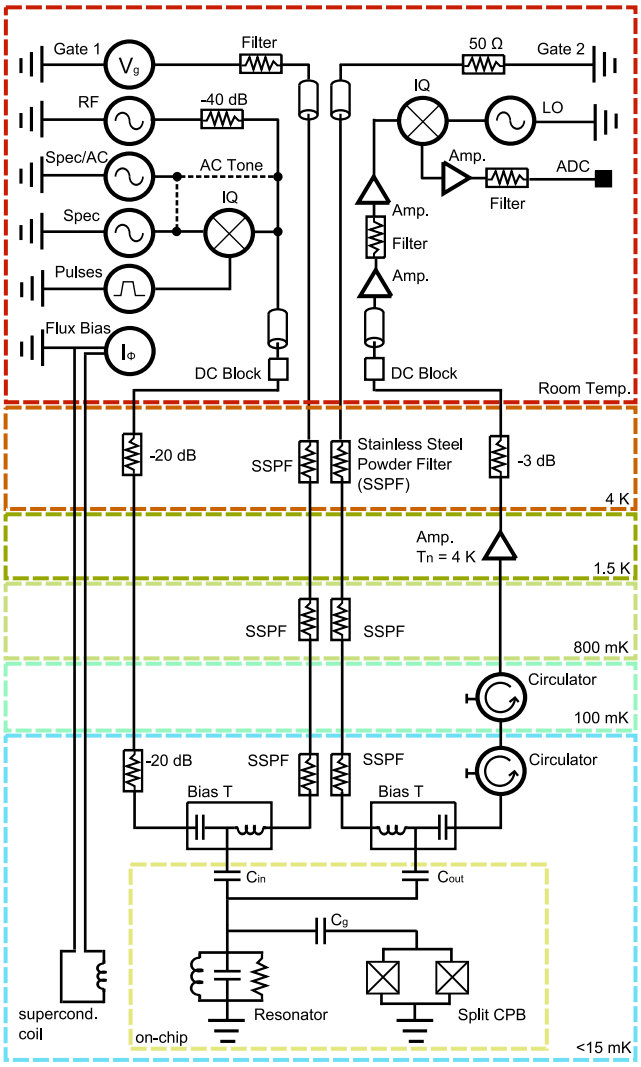


Fig. 3.2: Schematics of the measurement setup. The top left section shows the instruments on room temperature used to generate microwave signals, DC gate sweeps and DC current for the magnetic field. The microwave signal is modulated, filtered, attenuated and thermally connected to the different temperature stages in the cryostat on the way down to the sample. The DC gate signal is low pass filtered with copper powder filters and joined with the microwave signals using a bias-tee. After interacting with the sample, the transmitted signal is sent through two circulators that block the noise from the 1 K amplifier. It is then amplified with this cold low noise amplifier at 1 K and sent to room temperature where it is amplified and down converted with an IQ mixer to an IF signal before being digitally acquired. Taken from [29]

superconducting energy gap which is around 2.3 Kelvin in our case. A Kelvinox 400HA dilution refrigerator from Oxford Instruments capable of reaching a base temperature of ∼20 mK was used, which is colder then everywhere in the whole universe. The sample is shielded against electro magnetic radiation from thermal and other sources, which could cause unwanted qubit transitions. For detailed description of the design and operation of the dilution refrigerator see [33].

For the wiring, the amount of heat and electrical noise transfered along the cable down to the sample has to be minimized in order to ensure that the heat load does not harm the proper operation of the cryostat. For the microwave lines, the electrical noise is filtered by attenuating the signal. From room temperature (300 K) to liquid helium temperature (4 K), a 20 dB attenuator, and from liquid helium to base temperature (20 mK) another 20 dB of attenuation are used. This yields together with the attenuation of the cables about 50 dB of total attenuation. For the way back from the sample to room temperature the electrical noise added to the signal and the attenuation must be minimized. The signal is amplified with a low noise amplifier at 1 K. In order to avoid amplifier and thermal noise from the 1 K stage coming back to the sample, the signal between the sample and the amplifier is directed through two circulators. For the DC lines different technics to filter the noise are used. Since only a small bandwidth is needed, the signal can just be low pass filtered with copper powder filters, which has little attenuation at DC, but large attenuation at RF frequencies. To reduce the amount of heat transfered down to the sample, all lines are thermally anchored at the subsequently lower temperature stages in the dilution refrigerator.

## 3.4 Data acquisition

As discussed in Sec. 2.3.3, the qubit state is read out with the phase or amplitude of a microwave signal transmitted through the resonator at its resonance frequency $\sim 5$ GHz. The Nyquist-Shannon sampling theorem states, that a signal can be reconstructed exactly only if the sampling rate is greater or equal to twice the signal bandwidth. In order to acquire our signal digitally on a computer, we would need an acquisition card with a sampling rate of 10 GHz and above, which is difficult and expensive to achieve. Therefore, the signal is down-converted to a lower frequency first. This is done with an image rejecting IQ mixer where the measurement signal is mixed with a separately generated local oscillator (LO) signal with a frequency offset of $\omega_{IF}$. The amplitude and phase of the original signal are mapped onto two signals I and Q at frequency $\omega_{IF}$. The mixer can be operated in two different modes, if $\omega_{IF} = 0$ the measurement is called homodyne whereas if $\omega_{IF} \neq 0$ it is called heterodyne. Both channels are then amplified, low pass filtered and then digitized by an ADC acquisition card.
This card with a sampling rate of 1 Gs for each of two channels is able to acquire both quadratures I and Q simultaneously. An onboard FPGA allows to average the signals in real time which is needed due to the huge amount of data being accumulated during

the measurement. The memory of 24 bits (2 Mpoints) allows up to 65'000 averages to be taken at the full sampling rate with a resolution of 8 bits.
Once the data has been acquired, the phase and amplitude information is extracted. In the homodyne case, this is done using Eq. (3.2) and Eq. (3.3). This method has the advantage of high temporal precision which is limited only by sampling rate of the acquisition card and the bandwidth of the mixer and amplifiers that is around 350 MHz. Also the original signal can directly be observed without any post processing on a single channel, if the correct relative phase between the RF and the LO source has been chosen. The DC signals however are susceptible to 1/f noise and slow drifts. That's why the measurements are normally done in the heterodyne way with an IF frequency high enough to avoid 1/f noise, in our case 10 MHz. There are two possibilities to reconstruct the amplitude and phase in this case, either by just using one single I/Q branch or using both. The former is a good way to avoid errors due to any phase and amplitude imbalances between the two IQ arms of the mixer. In order to reconstruct the amplitude and phase exactly, the IF signal is averaged over one period, which reduces the bandwidth down to the IF frequency of 10 MHz. Why not just increase the IF frequency one might think. This would lower the number of points for the digital average process over one period which in turn reduces the accuracy of amplitude and phase. The 10 MHz has found to be a good compromise to be used. Using both channels, the bandwidth is limited as in the homodyne case only by the mixer or amplifiers, errors induced by imbalances in the mixer however have to be considered.

# 4 Measurements

The main goal of the measurements presented here is the measurement of the photon number inside the cavity with a Ramsey fringe type measurement of the ac-Stark shifted qubit transition frequency. This needs several measurements done first, such as the characterization of the sample parameters which is described in the first section. When all parameters of the qubit are tuned appropriately the ac-Stark shift of the qubit transition frequency due to the interaction with intra-cavity photons can be observed. In Sec. 4.2, time resolved measurements of the qubit state are presented. This includes the Rabi oscillation experiments, which enables the implementation of two important quantum gates, namely the bit-flip and the Hadamard gate, and allows to analyze the $T_1$ relaxation time of the qubit. To learn about the dephasing time $T_2$ and for the preparation of the final measurement, a Ramsey experiment is carried out. In the last section we present the first steps towards a possible implementation of a phase gate using the ac-Stark effect. The phase accumulated is controlled by populating the cavity with a certain amount of photons with an off resonant microwave pulse applied to the cavity. We discuss how the accumulated phase by such a pulse can be measured with a Ramsey type experiment and how to reconstruct from this measurement the average number of photons that were present in the cavity during the microwave pulse. The characterization of the qubit and some time resolved measurements have already been carried out by Johannes Fink during his diploma thesis [29] and some of the presented data are taken from his measurements.

## 4.1 Sample characterization

In order to perform the measurements, it is important to know all important parameters of the sample. This includes the resonance frequency $\omega_r$ and Q-factor of the cavity, the two characteristic energies $E_J$ and $E_C$ of the qubit that determine the transition frequency, as well as the coupling strength $g$ of the electro magnetic field to the qubit. This sections describes how to determine those parameters.

### 4.1.1 Cavity

The power transmitted trough the resonator at a driving frequency $\omega$ is as for all driven linear oscillators given by a Lorentzian that is centered around its resonance frequency

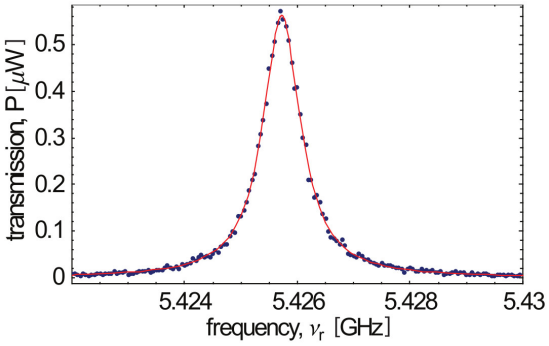


Fig. 4.1: Measured transmission power spectrum of our resonator. The solid red line is a fit to a Lorentzian line.

$\omega_r$

$$P(\omega) = P_0 \frac{\delta\omega^2}{(\omega - \omega_r)^2 + \delta\omega^2}, \tag{4.1}$$

where $\delta\omega^2$ is the half width at half maximum (HWHM) and $P_0$ the transmitted power on resonance. The phase shift $\Phi$ of the transmitted signal relative to the driving field is

$$\Phi(\omega) = \arctan\left[\frac{\omega - \omega_r}{\delta\omega}\right]. \tag{4.2}$$

In order to measure the power spectrum an RF signal is applied to the input capacitor of the resonator with a constant output power of the signal generator of $-38\,\mathrm{dBm}$, while the frequency is swept from $5.422\,\mathrm{GHz}$ to $5.43\,\mathrm{GHz}$, see Fig. 4.1. The transmitted signal is measured in heterodyne mode as described in Sec. 3.2 and averaged 2'000 times for each data point. Fitting the data with the Lorentzian (4.1) leads to a resonance frequency of $\omega_r/(2\pi) = \nu_r = 5.42472\,\mathrm{GHz}$ and a cavity decay rate $\kappa/(2\pi) = 2\delta\nu^2 = 0.83\,\mathrm{MHz}$ which corresponds to a quality factor of $Q = 6537$. This means the photons have a cavity life time of $T = 1/\kappa \approx 200\,\mathrm{ns}$ bouncing back and forth between the two capacitors of the resonator on average $Q/2\pi \approx 1000$ times.

### 4.1.2 Cooper pair box

We have already seen in Sec. 2.3 that the resonator frequency is shifted from the bare resonance frequency $\omega_r$ to a frequency $\omega_r' = \omega_r \pm \chi$, where the sign is determined by the state of the qubit. The dispersive shift $\chi = g^2/\Delta$ depends on the qubit detuning from the cavity $\Delta$ and the coupling strength $g$. The latter is completely determined by the fabrication parameters of the Cooper pair box, while the detuning can be varied by tuning the qubit transition frequency $\omega_a$ with either gate voltage or flux. This shift can be measured by the phase of a microwave signal transmitted trough the cavity on the bare resonance frequency. It is small for large detunings, gets larger when $\omega_a$ approaches

$\omega_r$ and changes its sign during the crossing of the resonator frequency. By analyzing the transition frequency of the qubit in dependence on the flux and gate charge, this sign change can be visualized as the intersection of this landscape with a plane at constant $\omega = \omega_r$, see Fig. 4.2(b). The resulting measurement response of the phase $\Phi$ to a gate and flux sweep is shown in Fig. 4.2(a). One can observe periodicity along both the flux and gate axis, which comes from the quantized nature of the flux through the loops of the CPB and of the charge on the island. The length of periodicity is exactly one flux quantum (corresponds to 86 $\mu$A through a superconducting coil) and respectively two elementary charges (404 mV at the DC input line).

The transition frequency at the sweet spot $n_g = 1$ is completely determined by the Josephson energy $\hbar\omega_a = E_J = E_J^{max}|\cos(\pi\theta/\theta_0)|$ with $\theta/\theta_0$ being the magnetic flux in units of the flux quantum $\theta_0$. It reaches its maximum at the points where the flux is an integer multiple $n$ of the flux quantum $\theta = n\theta_0$ and is equal to $\omega_a^{max} \approx E_J/\hbar$. Since the Josephson energy in our sample is smaller then the resonator frequency $E_J/\hbar < \omega_r$ it is not possible to tune this qubit to resonance with the resonator at the sweet spot. The detuning at those points is $\Delta = 1.7$ GHz which is far enough from the resonance frequency to work in the dispersive regime. The flux is for all further measurements tuned to one of those points.

To understand the response of the measurement better we look at the gate sweep for a fixed flux where the transition frequency at the sweet spot is maximal. The measured phase $\Phi$ and amplitude $A$ are shown in Fig. 4.2(b) and (c). When the gate voltage is increased such that the qubit frequency approaches the resonator frequency, the phase shift of the transmitted measurement signal increases. When the transition frequency of the qubit crosses the resonator frequency, the dispersive shift $g^2/\Delta$ and therefore also the measured phase changes their sign. At the degenerate point $n_g = 1$ the transition frequency reaches its minimum and approaches again from below the resonator frequency with increasing gate voltage. The two peaks where the phase changes its sign can therefore act as a "marker" to find the sweet spot which is exactly in the middle between them. Fitting the phase/amplitude response to such a gate voltage sweep allows one to determine the coupling strength $g/2\pi = 20$ MHz.

We have noticed that the qubit switches back and forth between the actual state and a state which is offset by exactly one electron charge. It can be seen in Fig. 4.2(a) as a weak shadow around $n_g = 2$ for low B-fields, and disappears for higher fields. Quasi particles tunneling from the island through the Josephson junction may be the reason for this behavior. Since it is a very weak effect, this effect did not harm our initial measurements. However, after we warmed up and cooled the sample down again one month later after a technical problem with the dilution refrigerator, another unstable offset-charge appeared which was not B-field dependent, see the gate sweep Fig. 4.3(a) and (b). The qubit switched now with equal probability between two states that are separated by only 0.08

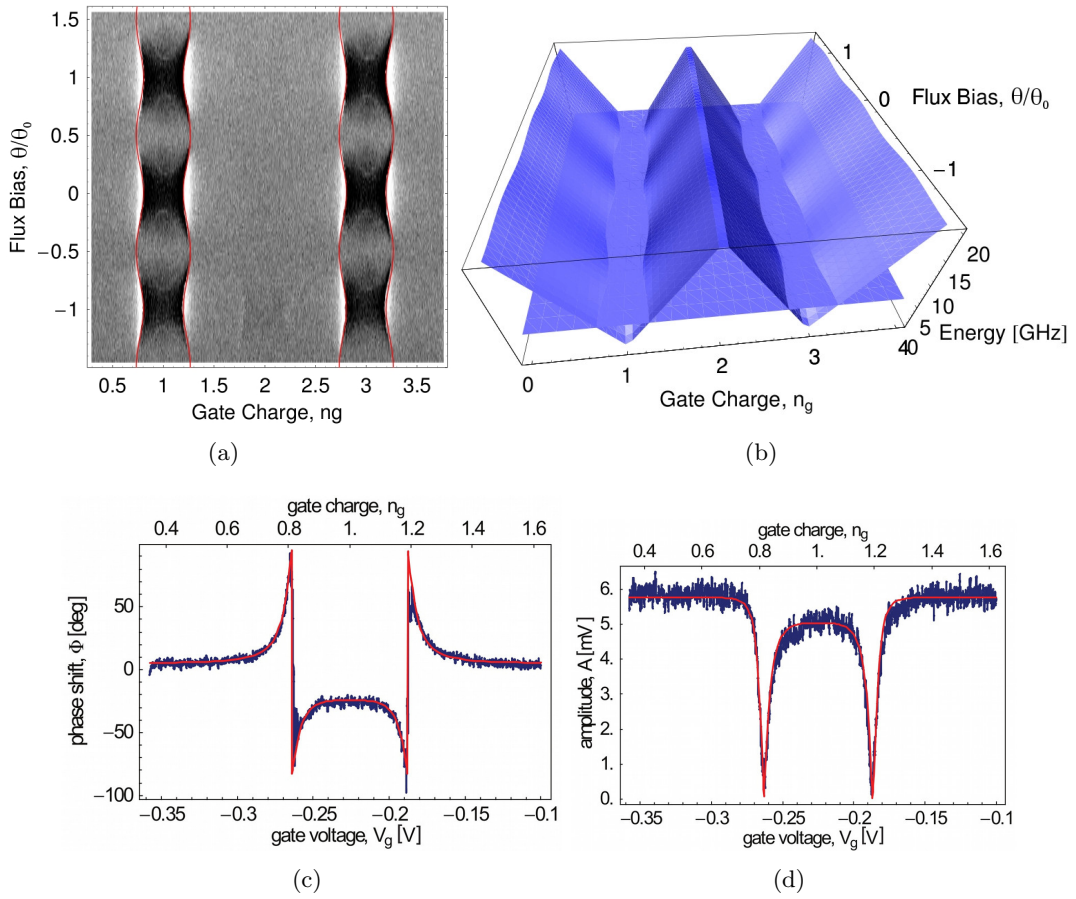


Fig. 4.2: **a)**Measured phase response of a measurement signal at the bare resonance frequency to a flux and gate sweep. Data taken from [29]. **b)** Theoretical landscape of the qubit transition frequency as well as the plane of the resonator frequency. The intersection of the plane with the landscape is indicated in a) with the red lines [29]. **c,d)** Measured phase respectively amplitude of the transmitted microwave in dependence on gate voltage for a fixed flux equal to an integer multiple of a flux quantum. The red curve indicates the theoretically calculated response.

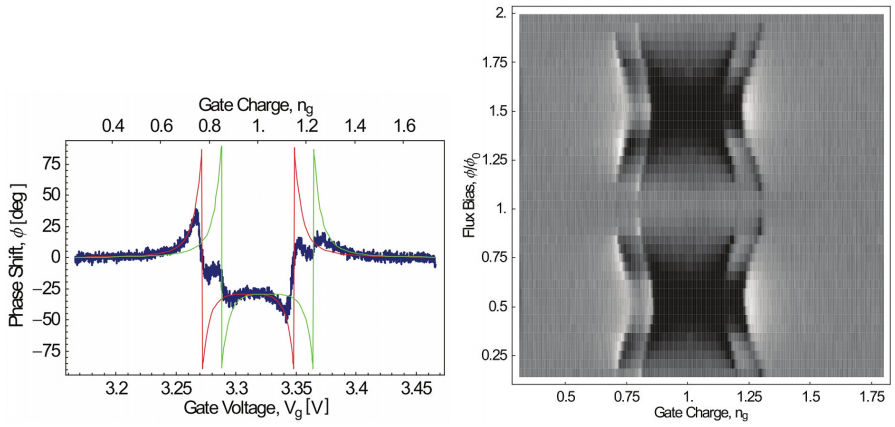


(a) (b)

Fig. 4.3: **a)** Measured phase $\Phi$ of the transmitted microwave in dependence of gate voltage for a fixed flux equal to an integer multiple of a flux quantum. Two theoretical response shifted by 0.08 elementary charge (red and green) are laid over the measurement, indicating the switching of the qubit in gate charge after a second cool-down. **b)** Density plot of the measured phase $\Phi$ vs. gate charge and flux bias. The two offset charge configurations are very stable and do not disappear for higher b-fields.

elementary charges in the gate voltage. Both theoretical measurement responses for the different states (red and green) are laid over the measurement. The reason for this offset-charge switcher is not known, we believe it could come from some parasitic charge located close to the CPB in the insulting material. Normally such switchers disappear after waiting some time when the qubit is at base temperature, or after warming up to 100 Kelvin and cooling down a second time. In our case however it did not. We have tried several other things, like applying gate voltages up to 8 Volts or high B-fields (up to 3 mA $\sim 35\theta_0$ through the superconducting coil), which did not help. This is the reason why we could not finish the implementation of the phase gate. All the measurements shown are done before this offset-charge instability appeared.

### Spectroscopy

Applying an additional spectroscopy tone in resonance with the qubit frequency allows to induce transitions between the two qubit states. When it is a continuous tone, the qubit transition saturates and the populations in the excited and ground state approach 1/2. Sweeping the spectroscopy frequency $\omega_s$ and the gate charge $n_g$ while measuring continuously the phase $\Phi$ of a measurement signal, the energy level separation $\omega_a$ of the qubit in dependence of the gate charge was measured, see Fig. 4.4(b). The resulting curve can be thought of as the intersection of the transition frequency landscape with a

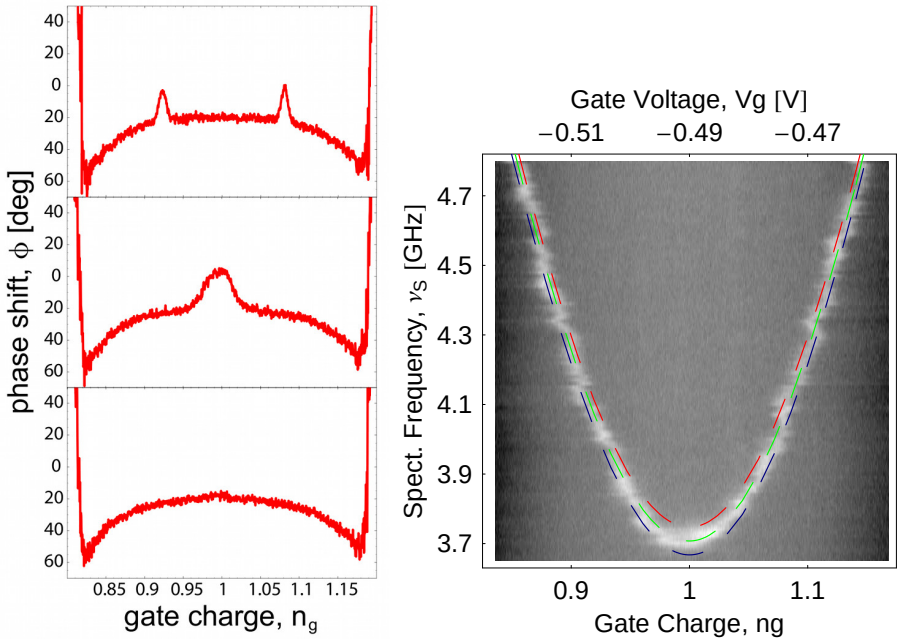


(a) (b)

Fig. 4.4: **a)** Measured phase shift $\Phi$ vs. gate charge $n_g$ while continuously applying a spectroscopy tone below (bottom), on (middle) and above resonance for $n_g = 1$ with the qubit. **b)** Density plot of the phase shift $\Phi$ vs. gate charge $n_g$ and spectroscopy frequency $\nu_s$. The curve of the phase peaks is a direct measure of the qubit transition frequency. Data taken from [29].

plane at constant flux. For the non resonant case, where $\omega_s < \omega_a$, the measured phase shift is as expected the same as if no spectroscopy pulse was applied, see Fig. 4.4(a) lower panel. The middle panel of Fig. 4.4(a) shows the case, where the spectroscopy microwave at $\nu_s = \omega_s/2\pi = 3.708\,\text{GHz}$ is in resonance with the qubit at the sweet spot $n_g = 1$, populating the excited state and thus inducing an additive peak saturating at 0 degree phase shift around the sweet spot. Increasing $\omega_s$ to higher values, resonance with the qubit occurs for two different $n_g$ that are located symmetrically around $n_g = 1$, inducing two separate peaks in the phase (see upper panel of Fig. 4.4(a)). The minimum of this spectroscopy curve allows to determine the qubit transition frequency up to several MHz accuracy, and thus to calculate $E_J^{max}/\hbar = 3.708\,\text{GHz}$. Fitting the whole spectroscopy curve gives a good estimate of the charging energy $E_C/\hbar = 5.25\,\text{GHz}$.

### 4.1.3 Ac-stark effect

So far we have discussed how the qubit state influences the properties of the cavity. In this section, the effect of the cavity photons on the qubit will be investigated. For

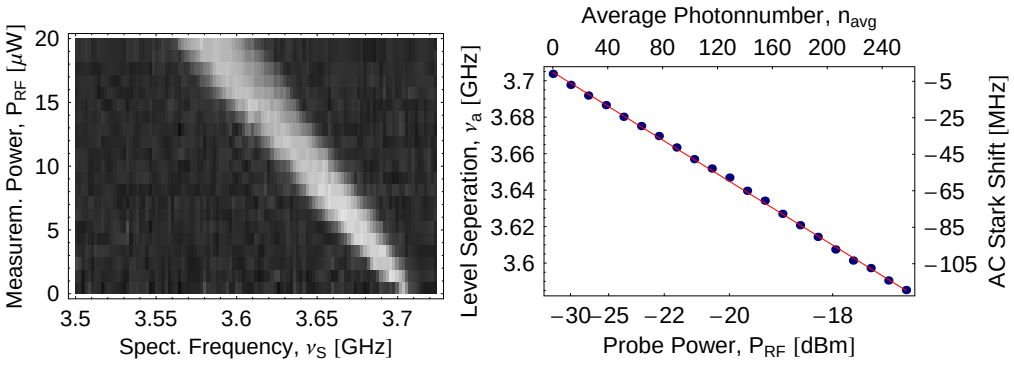


(a) (b)

Fig. 4.5: **a)** Density plot showing the transmitted phase shift as a function of spectroscopy frequency and measurement power. The center of the dip corresponds to the qubit transition frequency that is ac-Stark shifted with increasing measurement power. **b)** Qubit transition frequency extracted from a) as a function of measurement power. One observes the linear behavior for a wide range of measurement photon numbers (red is a linear fit). Data taken from [29].

this purpose we recall the Jaynes-Cummings Hamiltonian in the dispersive limit from Sec. 2.3

$$H \approx \hbar\omega_r \left(a^\dagger a + \frac{1}{2}\right) + \frac{\hbar}{2}\left(\omega_a + \frac{2g^2}{\Delta}a^\dagger a + \frac{g^2}{\Delta}\right)\sigma_z. \tag{4.3}$$

The qubit transition frequency in the resonator is given by the so called dressed qubit frequency $\omega_a + \frac{2g^2}{\Delta}a^\dagger a + \frac{g^2}{\Delta}$ which is shifted proportional to the photon number inside the cavity $\bar{n} = \langle a^\dagger a \rangle$ by the amount $2\chi = \frac{2g^2}{\Delta}$. The mean photon number $\bar{n}$, and therefore also the ac-Stark shift, is proportional to the input power of the measurement drive through the relation $P = \hbar\omega\bar{n}\kappa$, with $1/\kappa$ being the photon lifetime of the cavity. In Fig. 4.5 the spectroscopically measured line shape of the qubit in dependence on the measurement power is shown. With the knowledge of the coupling strength $g$ and the detuning $\Delta$, the ac-Stark shift of one photon is determined to be $2\chi = 2\pi\ 0.46\,\mathrm{MHz}$. Together with the measurement, this provides a possibility to perform a calibration of the measurement power needed to populate the cavity with one single photon, which in our case is $-41\,\mathrm{dBm}$.

Besides the ac-Stark shift, another effect can be observed in Fig. 4.5. As measurement power is increased, the line width of the qubit is broadened indicating an increase of the qubit dephasing rate. Quantum fluctuations of the photon number of the coherent microwave field lead to random fluctuations in the qubit transition frequency and therefore to a higher dephasing rate [34]. For more details see Sec. 4.3.2.

## 4.2 Coherent manipulations of the CPB state

We have so far only discussed time-independent spectroscopic measurements not considering time-resolved measurements of the qubit state. A first step towards quantum information processing with the CPB as a qubit is the ability to have full coherent control over the state of one single qubit. In order to accomplish this, one has to realize so called quantum gates that transform the qubit state coherently into another, or to speak in the Bloch sphere picture, that perform coherent rotations on the Bloch sphere. We discuss in this section the Rabi oscillation experiments in which rotations of the Bloch vector around the x- or y-axis are realized and show the Ramsey fringe experiment to measure the phase between the two qubit states. Both is needed to implement a phase gate (rotation around the z-axis) and to perform the measurement of the intra-cavity photon number present during the microwave pulse applied to the cavity for the phase gate. The coherent evolution of the qubit is however disturbed. Since our qubit is a macroscopic solid state device, it couples strongly to its environment which induces energy relaxation as well as dephasing of the qubit state. In order to implement quantum gates, both decoherence times must be significantly higher then the gate duration. We present the measurement of both, the relaxation and dephasing times $T_1$ and $T_2$ which were measured in Rabi oscillation and Ramsey fringe experiments. All measurements were performed in the dispersive limit, with the gate charge set to the sweet spot and the B-field set to a value that corresponds to an integer number of flux quanta.

### 4.2.1 Rabi oscillation

The qubit can be controlled coherently by applying microwave pulses to the input port of the resonator with frequency $\omega_s$, which are resonant or nearly resonant with the qubit transition frequency $\omega_a/(2\pi) \approx 3.708\,\mathrm{GHz}$. They induce periodic transitions between the qubit states called Rabi oscillation [35]. The probability to find the qubit in the excited state $|e\rangle$ oscillates with the Rabi frequency $\Omega_R$, whose value gives a measure for the coupling strength between the qubit and the quantized electromagnetic field. The corresponding quantum dynamics is described by the unitary transformation

$$U(t, t_0) = e^{-i(t-t_0)\frac{\Omega_R}{2}\sigma_x}, \tag{4.4}$$

and can be visualized in the Bloch sphere as a rotation around an axis that is defined to be the x-axis. In order to measure this process, the pulse sequence shown in Fig. 4.6(a) has been used. The qubit is first prepared in its ground state $|g\rangle$ by relaxation and then the Rabi pulse is being applied to induce the transition. During the whole sequence a weak (about 3 photons) continuous measurement signal with a frequency $\omega_{RF}$, which is on resonance with the resonator, was applied.

For the measurement shown in Fig. 4.6(b), this sequence was repeated every 110 $\mu$s, while the phase of the transmitted measurement signal was continuously monitored. The slow

repetition rate is used in order to ensure the complete relaxation of the qubit to the ground state. This was done several times for different Rabi pulse length $\Delta t$ from 0 ns to 40 ns, while the amplitude $A_s$ of the pulse is kept constant. The resulting change in the population (Fig. 4.6(c)) is an oscillatory function of $A_s$ and $\Delta t$, in agreement with the theory of Rabi oscillations [35]. The proportionality between the Rabi period and $A_s \Delta t$ was used to calibrate microwave pulses for the application of controlled rotations of the Bloch vector. For our configuration, a full rotation ($\Phi = 2\pi$) was found to correspond to a pulse with length of $\Delta t = 21$ ns and the Rabi oscillation rate is therefor $\Omega_R = \Phi/\Delta t \approx 0.3$ GHz.

Choosing the amplitude and length of the pulse such that it induces exactly a $\pi/2$ rotation respectively a $\pi$ rotation, the Rabi oscillation provides the possibility to implement two important single qubit gates in quantum information, the bit flip

$$\sigma_x = |0\rangle\langle 1| + |1\rangle\langle 0| = \begin{pmatrix} 0 & 1 \\ 1 & 0 \end{pmatrix} \tag{4.5}$$

respectively the Hadamard gate

$$H = \frac{1}{\sqrt{2}}(\sigma_x + \sigma_z) = \begin{pmatrix} 1 & 1 \\ 1 & -1 \end{pmatrix}. \tag{4.6}$$

The bit flip gate flips the state of a qubit from the ground to the excited state or vice versa. The Hadamard gate is used to create an equally weighted superposition of the two qubit states.

### 4.2.2 Measurement of the decoherence times

Starting from the ground state $|0\rangle$, it is possible to prepare the state $|1\rangle$ with the previously constructed bit-flip gate that performs a $\pi$ rotation of the state vector around the x-axis. Continuously measuring the state, the population peak height decays exponentially with the relaxation time $T_1$ (Fig. 4.7). By fitting the decay with an exponential we found a relaxation time $T_1 = 7.7\,\mu$s.

The dephasing of the qubit state can be analyzed with the so called Ramsey fringe experiment [36], that allows the measurement of the relative phase between two qubit states by interfering them with each other. Fig. 4.8(a) shows the microwave pulse sequence used for this measurement. Starting with the qubit in the ground state, one applies two Hadamard gates, i.e. two phase coherent microwave pulses corresponding each to a $\pi/2$ rotation ($\pi/2$-pulse) around a random axis that can be defined as the x-axis. They are slightly detuned from the transition frequency of the qubit by $\delta = \omega_a - \omega_s$ and are separated by a delay $\Delta t$. During this time, the state evolves freely and accumulates in the rotating frame of $\omega_a$ a relative phase $\phi = \delta \cdot \Delta t$. The first pulse brings the ground state in an equally weighted superposition state $1/\sqrt{2}\,(|0\rangle + |1\rangle)$, while the second pulse brings

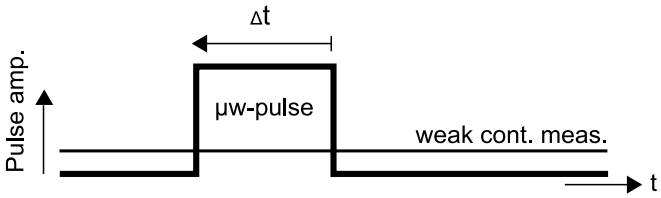


(a)

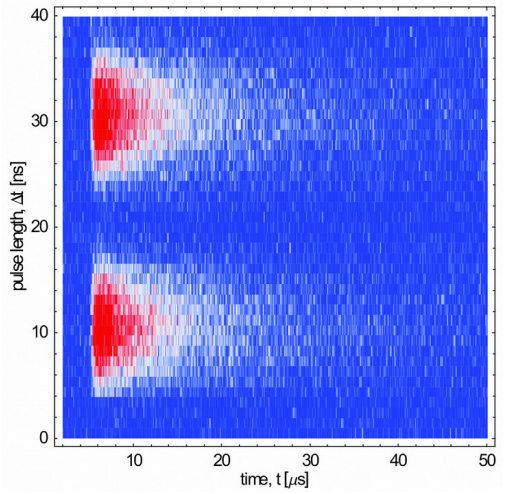


(b)

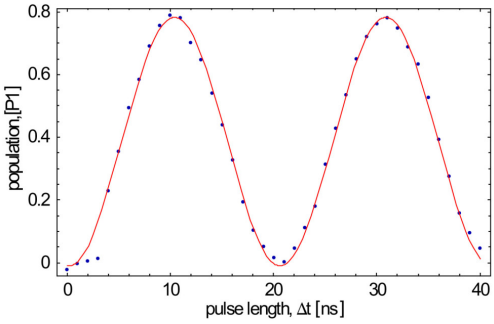


(c)

Fig. 4.6: **a)** Pulse sequence for the Rabi oscillation experiment with the Rabi pulse length $\Delta t$ and a weak continuous measurement signal at $\omega_r$. **b)** Color density plot of the measured phase $\Phi$ versus measurement time $t$ and Rabi pulse length $\Delta t$. **c)** Rabi oscillation in the qubit population $P1$ versus the $\Delta t$ (blue dots) and fit of the data with a sine function (red line).

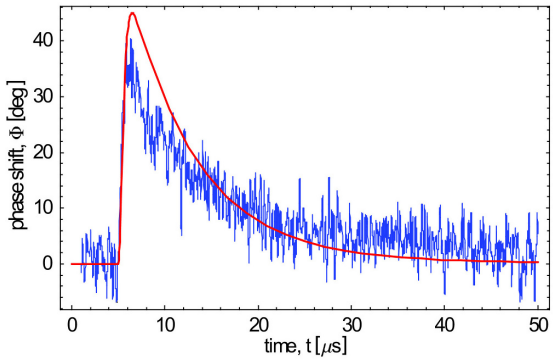


Fig. 4.7: Preparing the state $|1\rangle$ and measuring it continuously, shows an exponential decay of the state with time constant $T_1 = 7.7\,\mu$s. The red curve shows the expected response inferred from a cavity Bloch simulation.

it in a state whose projection on the z-axis is dependent on the accumulated phase during the time $\Delta t$. After those two pulses, a projective measurement is carried out which measures the z-component of the final state. It is turned on only after the second $\pi/2$-pulse in order to avoid dephasing induced by measurement photons inside the cavity.

This experiment is repeated for different delay times between $0 < \Delta t < 1.4\,\mu$s with a step size of 8 ns, while every measurement for a given $\Delta t$ was repeated and averaged 65'000 times. The measurement response is shown in Fig. 4.8(b). The population at time $t = 5\,\mu$s is extracted and plotted versus the delay between the two $\pi/2$ pulses. For a given detuning $\delta$, the population displays an oscillation at frequency $\delta$ which was set to 7.6 MHz in this measurement, see Fig. 4.8(c). Due to dephasing during the free evolution stage, the phase gets more and more unknown, leading to a exponential decay of the Ramsey fringes to a population of 0.5. Fitting the envelope of the oscillation yields to the dephasing time $T_2 \approx 700$ ns.

## 4.3 Photon number measurement with a Ramsey type experiment

We have already seen in the section about Rabi oscillations how to perform rotations of the qubit Bloch vector around the x or y-axis. In order to have full coherent control over the qubit state, one needs the additional ability to do rotations around the z-axis. The corresponding unitary operation for this process which adds a phase angle $\phi$ to the excited state component is called a phase gate

$$U(\phi) = |0\rangle\langle 0| + e^{i\phi}|1\rangle\langle 1| = \begin{pmatrix} 1 & 0 \\ 0 & e^{i\phi} \end{pmatrix}. \tag{4.7}$$

In this section we describe one possibility to implement a phase gate using the ac-Stark effect and present steps towards a measurement of the accumulated phase with a Ramsey type measurement. To perform this measurement it is necessary to carefully analyze microwave pulses applied to the cavity around its bare resonance frequency and the influence of photon number fluctuations on the dephasing of the qubit.

The ability to manipulate the transition frequency of a qubit with the ac-Stark effect provides a good method to implement a conditional phase gate [37]. As discussed in Sec. 4.1.3, each photon in the resonator on average increases the qubit frequency by the amount of $2g^2/\Delta$. This effect can be used to realize controlled rotation of the qubit about the z-axis by varying the number of photons in the resonator. The accumulated phase in the rotating frame of the qubit transition frequency $\omega_a$ is given by

$$\Phi(t) = \frac{2g^2}{\Delta}\int_0^t n(t')dt' \tag{4.8}$$

where $n(t)$ denotes the number of intra-cavity photons at time $t'$. The rate of this gate $\Omega_P = 2\bar{n}g^2/\Delta$ can be written in terms of the average number of photons $\bar{n} =$

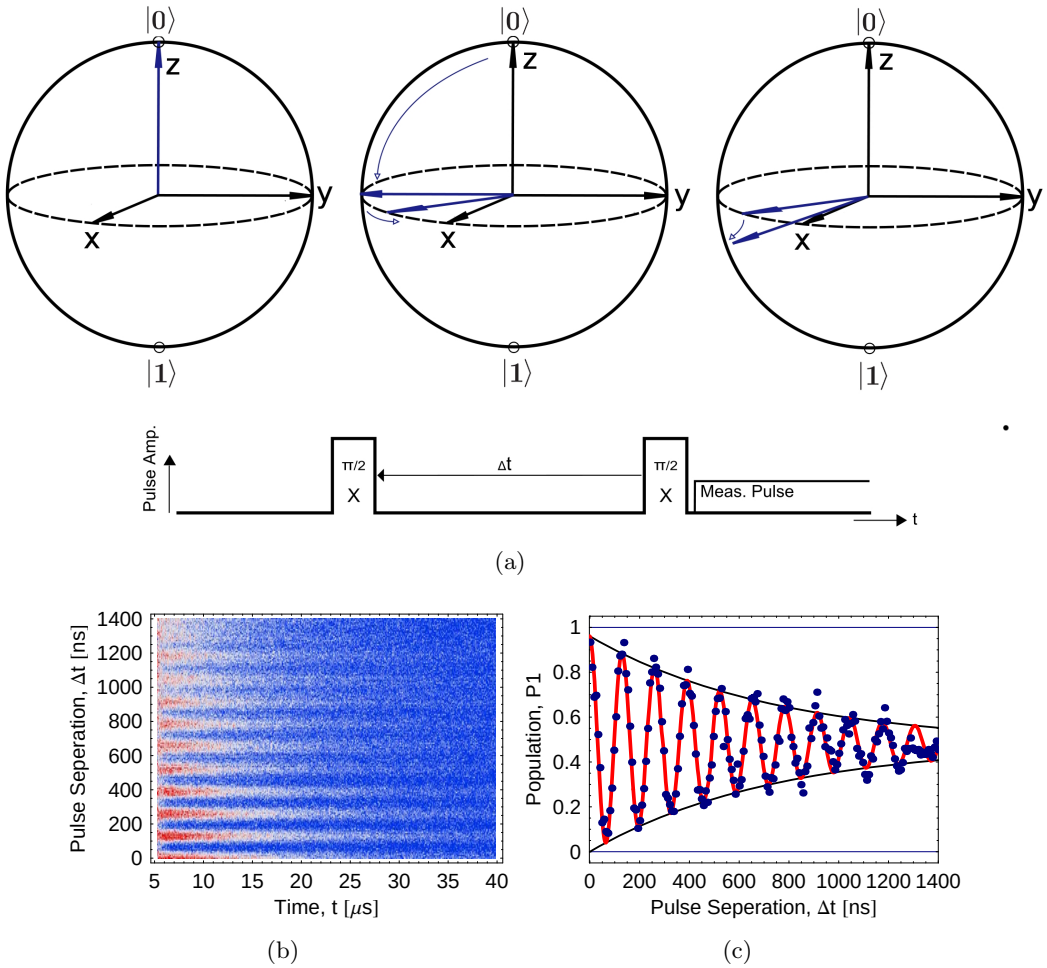


Fig. 4.8: **a)** Pulse sequence for Ramsey fringe experiment with pulse delay $\Delta t$ between two $\pi/2$ pulses and a pulsed measurement at the end. **b)** Density plot of the measured phase $\Phi$ versus the measurement time $t$ and $\Delta t$. **c)** Ramsey fringes of the qubit population $P1$ versus $\Delta t$. The red curve shows a fit to an exponentially decaying sine function. Data taken from [29].

$1/T \int_0^T n(t')dt'$ in the resonator, which is exactly the average qubit frequency shift induced by the ac-Stark effect. To realize fast rotation, one must therefore choose large $\bar{n}$ or large $g^2/\Delta$. Precise phase shifts can be induced by populating the resonator with a certain amount of photons with a pulsed microwave signal applied to the resonator at frequency $\omega_{RF}$. A phase sensitive measurement of the qubit state has been presented in the last section about Ramsey fringe oscillation. A similar experiment can be performed in order to measure the phase accumulated in a qubit state subject to such a microwave pulse and is explained next.

Fig. 4.9 shows the pulse sequence for this measurement. Starting with the qubit in its ground state, two phase coherent $\pi/2$ pulses on resonance with the qubit transition frequency $\omega_a$ are applied. The first pulse excites the qubit into the equally weighted superposition state $1/\sqrt{2}(|0\rangle + |1\rangle)$. In the rotating frame at the qubit frequency, the Bloch vector remains stationary. An additional microwave pulse applied to the cavity between the two $\pi/2$ pulses, I call it *ac-Stark pulse*, populates the cavity with a determined number of photons over a specific time interval which induces an ac-Stark shift of the qubit frequency and lets the Bloch vector precess around the z-axis in the rotating frame. The amount of phase accumulated during a whole ac-Stark pulse is determined by the integral in Eq. (4.8), which is exactly the area under the ac-Stark pulse, and can be tuned either by keeping the power of the pulse constant and changing its length $T$ or vice versa. The second $\pi/2$ pulse rotates the state vector such that the accumulated phase is mapped to the projection of the final state onto the z-axis. If one repeats this measurement several times with increasing the power or the length $T$ of the ac-Stark pulse, one ends up with an oscillation behavior similar to the Ramsey fringe experiment.

From this measurement, the average number of intra-cavity photons $\bar{n}$ populated by the ac-Stark pulse can be reconstructed. The accumulated phase is given by $\phi = \Omega_P T = 2T\bar{n}g^2/\Delta$ and the average photon number $\bar{n}$ can thus be calculated with $\bar{n} = \phi\Delta/T2g^2$.

In order to carry out this experiment, one has to consider a number of constraints:

- The maximal length of the whole pulse sequence should not exceed the dephasing time of the qubit (for our sample 600 ns) to maintain high visibility of the Ramsey oscillations.
- Careful analysis of the ac-Stark pulse is needed to realize short and well defined pulses. It turns out, that this is possible only by applying the pulses off resonantly, with a detuning $\Delta_d = \omega_{RF} - \omega_r$ much bigger then the cavity decay rate $\kappa$.
- One needs to realize pulses with high enough powers to get at least $2\pi$ phase shift with the minimal ac-Stark pulse length used. This is needed to see at least one full oscillation in the Ramsey type measurement. Since the Lorentzian spectrum of the resonator is falling off quadratically with the detuning for $\Delta_d \gg \kappa$ and the output power of our signal generators is limited to a maximum value of about 20 dBm, we had to limit ourself to a maximal detuning of $\Delta_d/2\pi = \pm 100$ MHz.
- Quantum fluctuations in the microwave field induce qubit level fluctuations leading to dephasing of the qubit state [37]. This back action of the photons around the

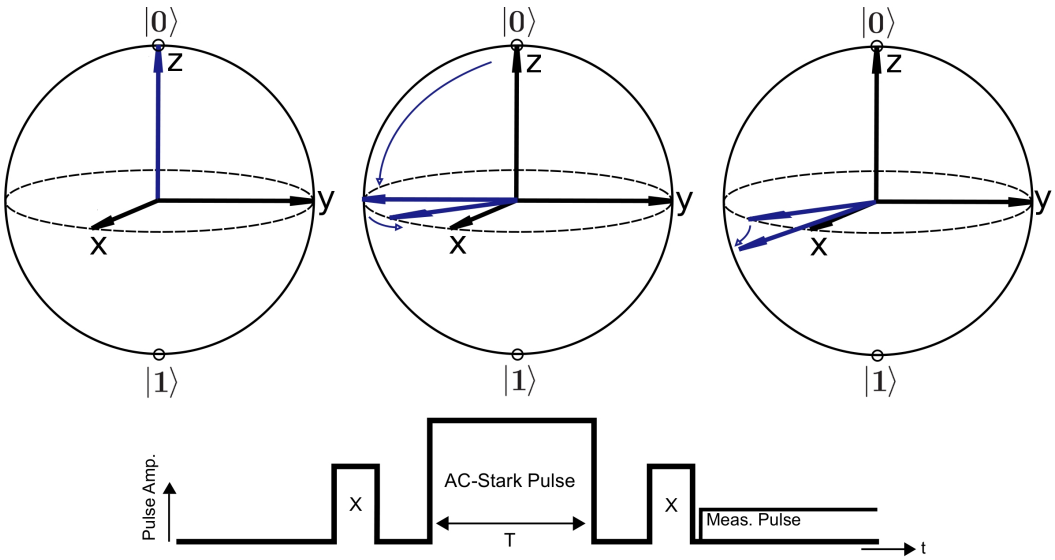


Fig. 4.9: Pulse sequence used for the Ramsey type measurement of the phase accumulated by an ac-Stark pulse (bottom). The corresponding qubit dynamics is visualized schematically with Bloch spheres in the rotating frame at the qubit transition frequency $\omega_a$(top).

resonator frequency on the qubit has to be determined and considered for an optimal choice of the ac-Stark pulse parameters.

### 4.3.1 Pulse analysis

A resonator driven with a microwave amplitude $V_{RF}$ can be modeled classically as an underdamped harmonic oscillator with resonance frequency $\omega_r$. The voltage $V$ inside the resonator is given by

$$V''(t) + \kappa V'(t) + \omega_r^2 V(t) = \frac{\partial}{\partial t} V_{RF}(t) \tag{4.9}$$

where $\kappa$ is the photon decay rate. The solution of this differential equation is a sum of a transient term that depends on the initial conditions, and a steady state term that is independent of the initial conditions and depends only on the driving frequency, driving amplitude, resonance frequency and the damping constant. For a driving field $V_{RF} = V_o \sin(\omega_{RF} t)$ the steady state solution is

$$V_{ss}(t) = B_1 \sin(\omega_{RF} t - \rho_1), \tag{4.10}$$

where $B_1^2$ defines the Lorentzian curve of the power transmitted through the resonator and $\rho_1$ is the phase of the transmitted signal relative to the driving field. For pulsed

driving of the resonator, the transient term has to be taken into account. The solution for an infinitely long square pulse, see Fig. 4.10(a), then

$$V(t) = B_1 \sin(\omega_{RF} t - \rho_1) + B_2 \sin(\omega_d t - \rho_2) \tag{4.11}$$

where

$$\begin{aligned}
\omega_d &= \sqrt{\omega_r^2 - \kappa^2/4}, \\
B_1 &= \frac{\omega_{RF} V_0}{\sqrt{\kappa^2 \omega_{RF}^2 + (\omega_{RF}^2 - \omega_r^2)^2}}, \\
B_2 &= B_1 \left(1 + \frac{\omega_{RF} - \omega_r}{\omega_d}\right) e^{-\kappa t/2}, \\
\rho_1 &= \arctan\left(\frac{\omega_{RF}^2 - \omega_r^2}{\kappa \omega_{RF}}\right), \\
\rho_2 &= \arctan\left(\frac{\kappa^2 + 2(\omega_{RF}^2 - \omega_r^2)}{2\kappa\omega_d}\right).
\end{aligned}$$

$\rho_2$ is the phase of the transient oscillation and its amplitude $B_2$ decays exponentially with time constant $\kappa/2$ and the solution becomes for long times $t$ the same as the steady state (4.10).
In order to measure this resonator response, the transmitted signal is mixed down in a homodyne way to its low frequency quadrature components $I(t) = V(t)\sin(\omega_{LO} t)$ and $Q(t) = V(t)\cos(\omega_{LO} t)$ with an image rejection IQ mixer where $\omega_{LO}$ is the frequency of the local oscillator. The mixer outputs are low pass filtered to remove the high frequency mixing products with frequency $\omega_{RF} + \omega_{LO}$. Those components are therefore dropped during the calculation of the two quadrature components $I(t)$ and $Q(t)$. The amplitude can then be reconstructed by summing the square of both components and taking the square root

$$\begin{aligned}
A(t) &= \sqrt{I(t)^2 + Q(t)^2} && (4.12) \\
&= B_1 \sqrt{1 + \frac{\omega_{RF}^2 \cdot e^{-\kappa t}}{\omega_r^2 - \kappa^2/4} - \frac{2\omega_{RF} \cdot e^{-\kappa t/2}}{\omega_d} \cos[(\omega_d - \omega_{RF})t + \rho_1 + \rho_2]}. && (4.13)
\end{aligned}$$

This solution is plotted in Fig. 4.10(b) with the parameters of our sample for a microwave frequency on resonance with the cavity (green dashed line) and for a detuning of 5 MHz (blue line). We discuss the solution in more detail in the following and present some measurements of the resonator response to such pulses.

### Resonant pulses

If the cavity is driven on resonance where $\omega_d - \omega_{RF}$ and the two phases $\rho_1$ and $rho_2$ are approximately zero, the cosine in Eq. (4.13) becomes approximately one. In this case

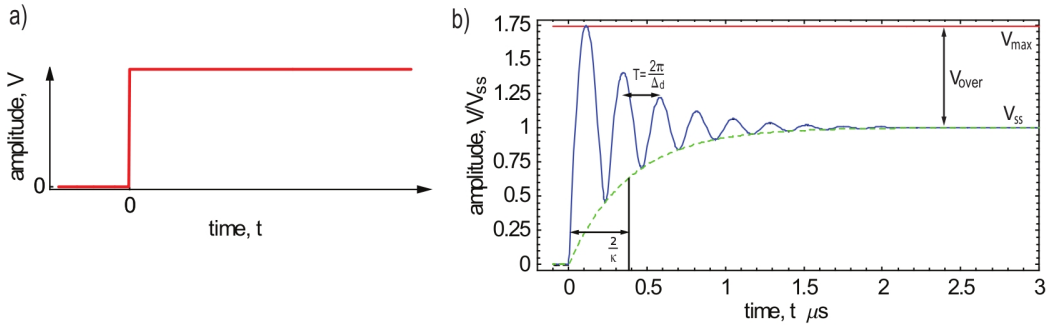


Fig. 4.10: **a)** Infinitely long microwave pulse with rectangular amplitude envelope starting at time $t = 0$. **b)** Simulation of the resonator response to an infinitely long microwave pulse at a detuning frequency $\Delta_d/2\pi = 5\,\mathrm{MHz}$ calculated with Eq. (4.13) (blue solid line) with the parameters of our sample. The transient part is oscillating at the detuning frequency $\Delta_d/2\pi$, thus has the period $T = 2\pi/\Delta_d$, and decays exponentially with time constant $2/\kappa$. The green dashed line shows the response on resonance.

the amplitude inside the resonator

$$A(t) \approx B_1(1 - e^{-\kappa t/2}) \tag{4.14}$$

rises exponentially with the characteristic time $2/\kappa$ to its steady state amplitude and decays exponentially when the driving pulse is turned off. We have measured the resonator response in this case in a homodyne way. The measured output power $P_{\mathrm{out}}$ of the resonator and the intra-cavity photon number as a function of time is shown in Fig. 4.11. The measurement power needed to populate the cavity on average with one single photon in the steady state was calibrated in Sec. 4.1.3. By determining the measured output power to such a measurement signal, we performed a calibration of the output power measured when the cavity is populated with a certain amount of photons. A fit of the data with Eq. (4.14) shows perfect agreement and yields a cavity decay rate of $\kappa/(2\pi) = 0.84\,\mathrm{MHz}$ which is the same as found with the spectroscopic measurement in Sec. 4.1.1. Due to the high quality factor of the resonator (small $\kappa$) the resonator reacts slow compared to the dephasing time of the qubit. It is therefore hard to populate the resonator with resonant photons on a short timescale. Large phase shifts can thus only be achieved by applying high input powers or applying off resonant pulses which is analyzed in the next paragraph.

### Off resonant pulses

If the driving pulses are applied with a frequency that is different from the resonance frequency, additional transient oscillations can be observed (see Fig. 4.11) that are coming from the cosine term in Eq. (4.13) which decay with the same characteristic rate

$\kappa/2$ as in the resonant case. They are present only during the driving of the resonator, as soon as the driving field is turned off they disappear and the amplitude decays exponentially with $\kappa/2$. The frequency of the transient oscillations is approximately the detuning frequency $\Delta_d = \omega_{RF} - \omega_r$ of the driving field from the resonance frequency. If the pulse length matches exactly an integer number $n$ of periods of the transient oscillation $T = n2\pi/\Delta_d$, the pulse ends at a minimum of the transient oscillation and very short pulses can be applied, see Fig. 4.12. If the pulse ends at the maximum, a lot of photons remain in the resonator which take a long time to leave. Therefore the best way to vary the intra-cavity photon number with a ac-Stark pulse is to vary the power while taking a constant pulse length $T = n2\pi/\Delta_d$. The relative overshoot $V_{\text{over}}$, which is defined as the difference between the maximum amplitude of the oscillation and the steady state amplitude, divided by its steady state amplitude, see Fig. 4.10(b) , can be approximated by $e^{(-\pi\kappa/(2\Delta_d))}$. For a detuning $\Delta_d \gg \pi\kappa/2$, the overshoot is $V_{\text{over}} \approx 1$, which means that the maximal amplitude of the transient oscillation is two times the steady state amplitude $V_{\text{ss}}$. This allows therefore to populate the resonator with up to 4 times more photons with a given power compared to the steady state.

Similar measurements have been carried out for Gaussian pulses as shown in Fig. 4.13, where the $\sigma$ is the variance when we look at the power of the pulse. The variance of the amplitude is given by $\sigma_{\text{amp}} = \sqrt{2}\sigma$. The response of the resonator on resonance is again a Gaussian curve for variances $\sigma > 1/\kappa$. For $\sigma < 1/\kappa$ however, the photons start to decay exponentially with decay rate $\kappa$ when the power of the driving field is under a certain threshold. Driving the resonator off resonant, the minimal variance $\sigma_{\text{min}}$ at which this exponential decay appears can be lowered significantly from 200 ns on resonance down to 10 ns at 100 MHz detuning. A Gaussian pulse with variance $\sigma = 100$ ns at a detuning of 10 MHz, see Fig. 4.13(a), shows no exponential decay, while at same detuning, a Gaussian pulse with $\sigma = 18$ ns does, Fig. 4.13(b). When analyzing the Fourier spectrum of the Gauss pulse, see Sec. 4.3.3, a good approximation for $\sigma_{min} \approx 2\pi/\Delta_d$ is found, provided that $\omega_d \gg \kappa$. An advantage of Gaussian pulses over square pulses is that they induce no dephasing of the qubit when applied off resonantly. This becomes clear after the discussion about the influence of intra-cavity photons on the dephasing of the qubit and the analysis of the pulses in the frequency spectrum. However, the Gaussian is a function that is rising/falling relatively slow. The time t until the power is fallen below one percent of the maximum power is given by $t = \sigma\sqrt{2\ln 100} \approx 3\sigma$, see Fig. 4.14, which makes the pulse sequence at least $6\sigma$ long. The minimal variance together with the fact, that the length of the pulse sequence scales fast with varying the variance, the best way to implement the ac-Stark pulse in the Ramsey type experiment is again to fix the variance and vary the power.

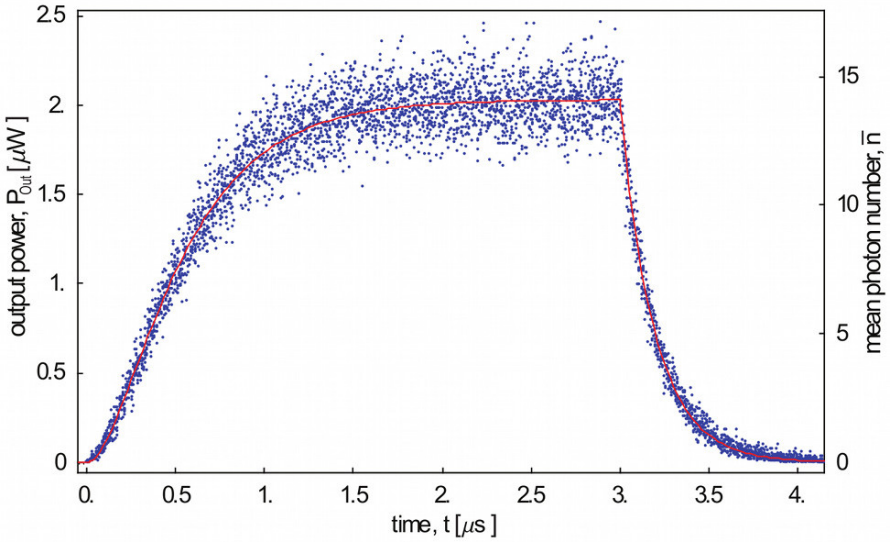


(a)

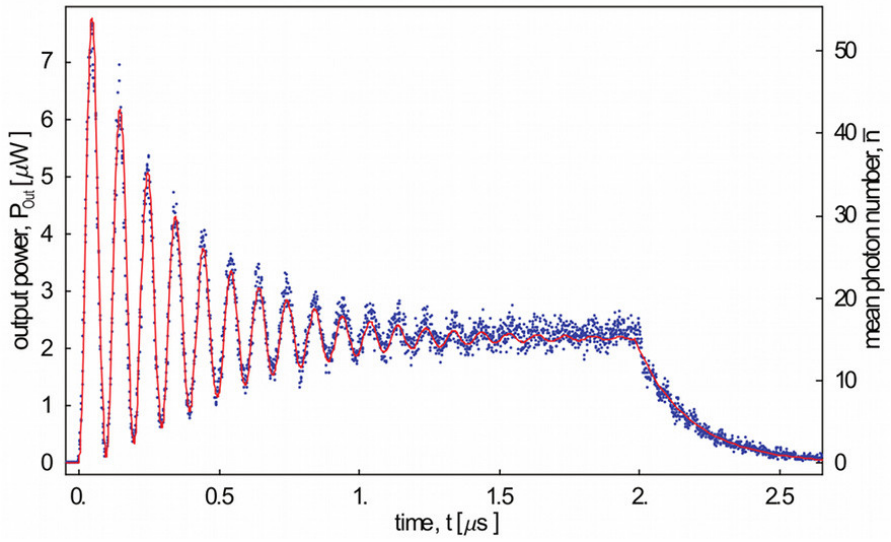


(b)

Fig. 4.11: Homodyne response of the resonator driven with a square pulsed microwave field whose frequency $\omega_{RF}$ is on resonance **(a)** and 10 MHz detuned **(b)** from the resonator frequency. The left axis shows the transmitted power through the resonator after all the amplification stages from the sample to the acquisition card. The right axis shows the average number of photons inside the resonator. The red solid lines are a fit of the data to the theoretical solution of a driven harmonic oscillator Eq. (4.13).

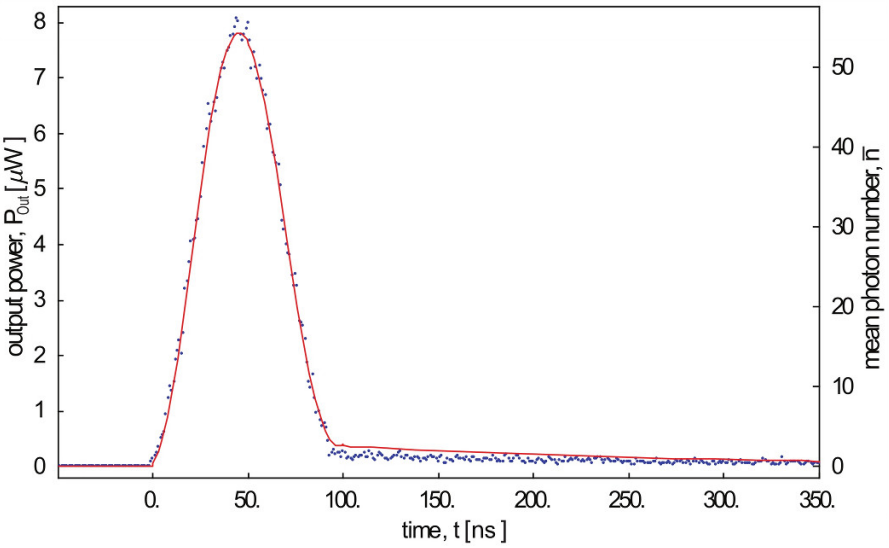


(a)

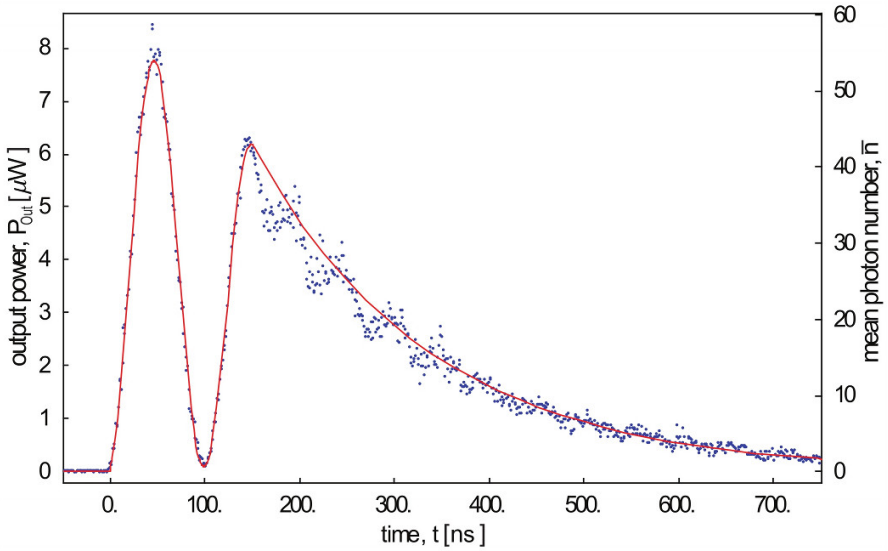


(b)

Fig. 4.12: This figure shows the homodyne response of the resonator driven with a square pulsed microwave field whose frequency is 10 MHz detuned from the resonator frequency. **a)** The pulse length of 100 ns corresponds to a multiple of the transient oscillation period and therefore ends at a minimum of the oscillation. **b)** The pulse with a length of 150 ns ends at a maximum of the transient oscillation and the remaining photons inside the cavity decay exponentially with rate $\kappa$. The red curve is a fit to Eq. (4.13)

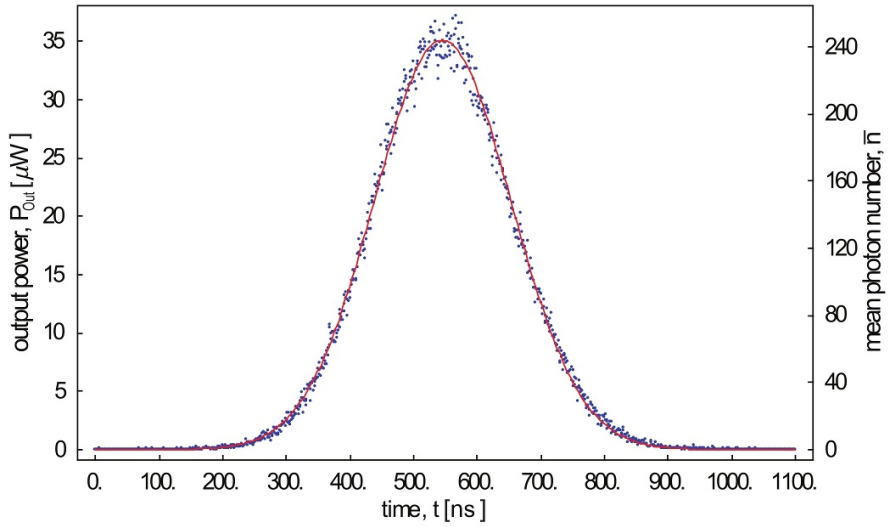


(a)

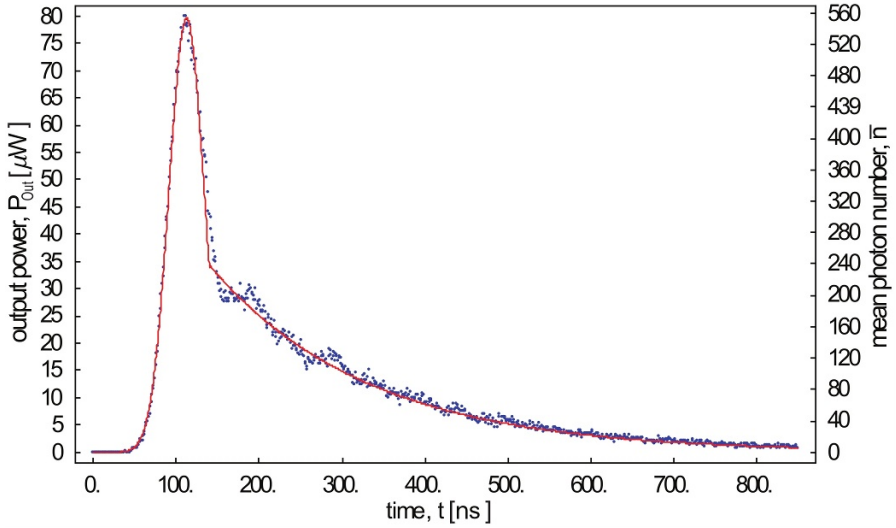


(b)

Fig. 4.13: Homodyne response of our resonator driven with a Gaussian pulse at 10 MHz detuning from the resonator frequency. The result for a variance of 100 ns is shown in **(a)** and for a variance of 18 ns in **(b)**. The red curve is a fit to a Gaussian for **(a)** and for **(b)** a fit to a Gaussian up to the time where it decays exponentially. From there, the data is fitted with an exponential.

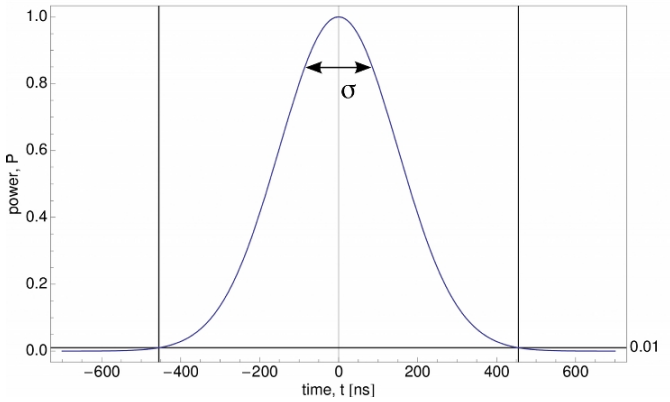


Fig. 4.14: Plot of a Gaussian with variance $\sigma = 150\,\text{ns}$. The two black lines at $t \approx \pm 450\,\text{ns}$ indicate how long it takes until the power of the Gaussian is fallen below one percent of the maximum power.

### 4.3.2 Photon induced dephasing

The cavity is populated with photons using a coherent field generated with a microwave source. The photon number undergoes quantum fluctuations (photon shot noise) $\delta n$ around the mean $\bar{n}$ obeying a Poisson distribution. This induces random fluctuations in the qubit transition frequency which leads to photon-induced dephasing of the qubit. However, the amount of the photon-induced dephasing depends strongly on the detuning of the photons from the cavity and can be neglected for high detunings [37]. This section covers a short theoretical summery of this effect.

By measuring the phase of a microwave beam transmitted through the cavity as a function of the excitation frequency of the qubit, one has access to the absorption spectrum of the qubit [38]

$$S(\omega) = \frac{1}{2\pi} \int_{-\infty}^{\infty} dt\; e^{i\omega t} \left\langle \hat{\sigma}_-(t)\hat{\sigma}_+(0) \right\rangle_s , \tag{4.15}$$

where the subscript s implies that the expectation value is taken in the steady state. $S(\omega)$ is the Fourier transform of the correlation function $\left\langle \hat{\sigma}_-(t)\hat{\sigma}_+(0) \right\rangle_s$. The dephasing rate can now be determined from the half width at half maximum of $S(\omega)$ [39]. The correlation function can be calculated in two ways [37] that are described in the following.

One way is the Gaussian approximation. Here the qubit is assumed to be in a superposition state $|\psi(0)\rangle = (|0\rangle + |1\rangle)/\sqrt{2}$ and the cavity is populated at its bare resonance frequency with an average photon number $\bar{n}$. As the qubit state evolves in time, it accumulates additional to the intrinsic phase a photon induced relative phase $\phi(t) = 2\chi\bar{n}t + 2\chi \int_0^t dt' \delta n(t')$ between the ground and the excited states, where $\chi = g^2/\Delta$

is the dispersive field/qubit coupling term. There is the first term which depends on the mean photon number, and the second term which is determined by the random fluctuations around the mean value. Following Ref. [37], the correlation function can be found to be

$$\langle \hat{\sigma}_-(t)\hat{\sigma}_+(0)\rangle_s \approx e^{-\gamma_2 t} \exp\left[2\chi^2 \int\int_0^t dt_1 dt_2 \, \langle \delta n(t_1)\delta n(t_2)\rangle\right] \tag{4.16}$$

where the fluctuations $\delta n$ are assumed to be Gaussian, and $\gamma_2$ is the intrinsic dephasing rate of the qubit. This expression involves the photon correlation function [28] $\langle \delta n(t_1)\delta n(t_2)\rangle = \bar{n}\exp(-\kappa|t|/2)$ which is governed by the cavity decay rate $\kappa$. Taking the Fourier transform of Eq. (4.16) results in the spectroscopic line shape of the qubit [37]

$$S(\omega) = \frac{1}{2\pi}\sum_{j=0}^{\infty} \frac{(-2\tilde{\Gamma}_m/\kappa)^j}{j!} \frac{\tilde{\Gamma}_j/2}{(\omega - \tilde{\omega}_a - 2\bar{n}\chi)^2 + (\tilde{\Gamma}_j/2)^2}, \tag{4.17}$$

where $\tilde{\Gamma}_j = 2(\gamma_2 + \tilde{\Gamma}_m) + j\kappa$, $\tilde{\omega}_a = \omega_a + \chi$ being the Lamb-shifted qubit transition frequency and $\tilde{\Gamma}_m \approx 4\bar{n}\chi^2/\kappa$ being the measurement induced dephasing rate in the small cavity frequency shift limit ($\chi \ll \kappa$) and for small photon numbers. From this equation we see that if the measurement rate $\tilde{\Gamma}_m$ is much smaller then the cavity decay rate $\kappa/2$, only few terms in the sum contribute and the spectrum is Lorentzian whose width is proportional to $\bar{n}$. For fast measurement rates on the other hand, the spectrum will be a sum of many Lorentzians, resulting in a Gaussian curve with variance proportional to $\sqrt{n}$. Therefore, for small photon numbers populating the cavity, the dephasing rate is $\propto n$ whereas for high photon numbers the dephasing scales as $\sqrt{\bar{n}}$. The half width at half maximum of Eq. (4.17) has been evaluated numerically from its analytic solution with the previously found parameters for our system, and plotted in Fig. 4.15 (red curve). For no intra-cavity photons, the total dephasing rate $\gamma$ is completely determined by the intrinsic dephasing rate $\gamma_2$ which we have found to be $\gamma_2 = 1.5\,\mathrm{MHz}$ for our system (Sec. 4.2.2). As the mean photon number $\bar{n}$ is increased, the dephasing rate increases first linearly with $\bar{n}$ and for higher powers with the square root of $\bar{n}$.

As discussed before, we need to apply off resonant pulses to the cavity in order for them to be short enough and well defined. Therefore, we would like to evaluate the influence of such pulses on the dephasing rate. The equation above however is derived with the assumption of photons at the bare resonance of the cavity. We have to go beyond the Gaussian approximation and derive the correlation function by solving the master equation of the qubit coupled to the environment with the positive P-function method [37]. The qubit plus the cavity system are described by a mixed state $\rho(t)$ whose evolution is given by the master equation [40]

$$\dot{\rho} = \mathcal{L}\rho, \tag{4.18}$$

$$= -\frac{i}{\hbar}[\mathcal{H},\rho] + \kappa\mathcal{D}[\hat{a}]\rho + \gamma_1\mathcal{D}[\hat{\sigma}_-] + \frac{\gamma_2}{2}\mathcal{D}[\hat{\sigma}_z]\rho, \tag{4.19}$$

where $\mathcal{D}[\hat{L}]\rho = \left(2\hat{L}\rho\hat{L}^\dagger - \hat{L}^\dagger\hat{L}\rho - \rho\hat{L}^\dagger\hat{L}\right)/2$. $\hat{L}$ are the so called Lindblad operators, representing the coupling of the system to its environment in the Born and Markov approximation. The last three terms of Eq. (4.19) correspond to loss of photons at rate $\kappa$, energy relaxation in the qubit at rate $\gamma_1$ and pure dephasing of the qubit at rate $\gamma_2$. Following the calculations from [37], one obtains the spectrum in the limit of $\chi \ll \kappa$

$$
\begin{aligned}
S(\omega) &= \frac{1}{\pi}\sum_{j=0}^{\infty}\frac{1}{j!}Re\left[\frac{(-A)^j e^A}{\Gamma_j/2 - i(\omega-\omega_j)}\right], && (4.20)\\
A &= D_s\frac{\kappa/2 - i\chi - i\Delta_r}{\kappa/2 + i\chi + i\Delta_r}, && (4.21)\\
D_s &= \frac{4\bar{n}\chi^2}{\kappa^2/4 + \chi^2 + \Delta_r^2}, && (4.22)\\
\Gamma_j &= 2(\gamma_2 + \Gamma_m) + j\kappa, && (4.23)\\
\Gamma_m &= \frac{D_s\kappa}{2}, && (4.24)\\
\omega_j &= \tilde{\omega_a} + B + j(\chi + \Delta_r), && (4.25)\\
B &= 2\bar{n}\chi - \chi D_s. && (4.26)
\end{aligned}
$$

In the small cavity frequency shift limit and for zero detuning ($\Delta_r = 0$), this equation is approximately the same as the Gaussian approximation Eq. (4.17) and we therefore get the same HWHM. For nonzero detuning however, the photon induced dephasing rate is only significant in a small frequency range around the bare resonance frequency of the cavity. Already for a detuning of 5 MHz $\approx 6\kappa/(2\pi)$ the photon induced dephasing can be neglected, see Fig. 4.15 (blue curve). The dephasing stays almost constant at $\gamma_2$ for the photon numbers $\bar{n}$ plotted. This can be explained with the Heisenberg type uncertainty relation between rate of information gain and dephasing. As we have seen earlier, the qubit pulls the resonator frequency up and down producing a state dependent phase shift of transmitted photons near the bare resonator frequency. But off resonant photons receive phase shifts nearly independent of the qubit state (see Fig. 2.13). These photons deliver almost no information about the qubit state, and hence do not contribute to dephasing.

### 4.3.3 Fourier analysis

In the last paragraph, we have seen that predominantly photons with a frequency of $\pm 6\kappa$ around the resonator frequency contribute to dephasing of the qubit. In this paragraph we analyze the microwave pulses used for phase shifting the qubit state in the frequency domain to determine the contribution of these photons to the qubit dephasing.
The pulses $f(t)$ can be mathematically represented by a product of two functions, one is the microwave signal $s(t) = \sin(\omega_0 t)$ and the other a window function $w(t)$ that modulates the signal. Here we consider either a rectangular function or a Gaussian

$$f(t) = w(t)s(t). \quad (4.27)$$

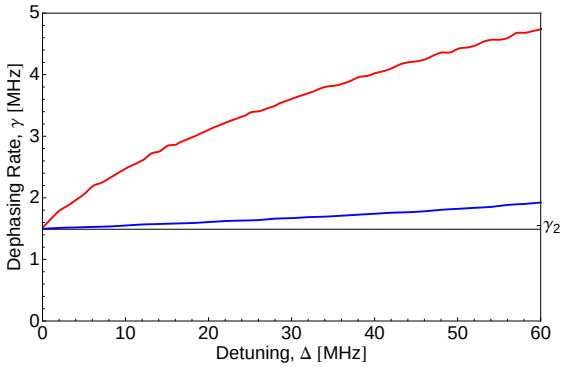


Fig. 4.15: Calculated half width at half maximum (HWHM) of the measurement broadened qubit spectrum as a function of the photon number $\bar{n}$. The parameters are the ones we have measured for our sample in the previous sections. The red curve is obtained from Eq. (4.17) for photons at the bare cavity resonance frequency, and the blue curve is calculated from Eq. (4.20) for photons at 5 MHz detuning from the bare resonance frequency.

To go from the time domain into the frequency domain, $f(t)$ is Fourier transformed as

$$\mathcal{F}[f(t)] = F(\omega) = \frac{1}{\sqrt{2\pi}} \int_{-\infty}^{\infty} f(t) e^{-i\omega t} dt = \frac{1}{\sqrt{2\pi}} \int_{-\infty}^{\infty} w(t) s(t) e^{-i\omega t} dt, \tag{4.28}$$

and can be written as the convolution of the two individual Fourier transforms $W(\omega)$ and $S(\omega)$

$$\mathcal{F}[w(t)s(t)] = \frac{1}{\sqrt{2\pi}} W(\omega) * S(\omega). \tag{4.29}$$

For a square or Gaussian pulse, the window function is

$$w_{\text{square}}(t) = \begin{cases} 1, & -T/2 \leqslant t \leqslant T/2 \\ 0, & \text{otherwise} \end{cases}, \tag{4.30}$$

$$w_{\text{gauss}}(t) = e^{-\frac{t^2}{2\sigma_{\text{amp}}^2}}, \tag{4.31}$$

and the Fourier transform for both cases becomes

$$F_{\text{square}}(\omega) = \frac{i}{\sqrt{2\pi}} \cdot \frac{(\omega+\omega_0)\sin[\frac{T}{2}(\omega-\omega_0)] - (\omega-\omega_0)\sin[\frac{T}{2}(\omega+\omega_0)]}{\omega^2-\omega_0^2}, \tag{4.32}$$

$$F_{\text{gauss}}(\omega) = \frac{i\sigma_{\text{amp}}}{2} e^{-\frac{1}{2}\sigma_{\text{amp}}^2(\omega+\omega_0)^2} \left(-1 + e^{2\sigma_{\text{amp}}^2\omega\omega_0}\right). \tag{4.33}$$

This is a complex function from which the Fourier Spectrum can be calculated with $A(\omega) = |F(\omega)|$ and the phase angle with $\Phi(\omega) = \arctan[\text{Im}(F(\omega))/\,\text{Re}(F(\omega))]$. One has

to note that the Fourier Spectrum consists of two components, one for positive and one for negative frequencies, that are symmetric around zero. In physics, only positive frequencies make sense. To get the correct power per frequency if one only looks at positive frequencies, the two components have to be added together before calculating the power spectrum and is then given by $S(\omega) = |2F(\omega)|^2$. The power spectrum as a function of frequency $\nu$ rather then angular frequency $\omega$ is found by $S(\nu) = 2\pi S(\omega)$ and plotted for a square pulse with a length of 100 ns and 150 ns in Fig. 4.16(a) and (c) at a detuning of 10 MHz. It is a squared sinc function that is offset along the frequency axis by the microwave frequency $\nu_0 = \omega_0/2\pi$. Its roots are given by $\nu_0 \pm \frac{n}{T}$, where $n = \pm 1 \cdots \pm \infty$. Comparing those results with the square pulse analysis in Sec. 4.3.1, we see that the resonator frequency $\nu_r = \omega_r/2\pi$ is exactly at a root of the power spectrum whenever the pulse length is taken such that it ends at a minimum of the transient oscillations. Is $\nu_r$ a maximum of the power spectrum, the pulse ends at a maximum of the transient oscillation. This can be explained by extracting the power spectrum of the pulse inside the resonator $\tilde{S}(\nu)$, which is calculated by multiplying the Lorentzian resonator curve $P(\nu)$ with the power spectrum of the pulse $\tilde{S}(\nu) = P(\nu)S(\nu)$, see Fig. 4.16. Power components for off resonant frequencies are attenuated significantly, since the input capacitor of the resonator reflects most of the input power. The power spectrum inside the resonator shows for the 100 ns pulse a wide distribution of the power around the microwave frequency $\nu_0$ with a root at the resonator frequency $\nu_r$, see Fig. 4.16(b). For the 150 ns pulse however, most of the power is concentrated around the resonator frequency, see Fig. 4.16(d). Those resonant photons are the ones contributing to the exponential decay with the characteristic decay rate $\kappa$ after turning off the driving field. The same effect can be observed for Gaussian pulses, see Fig. 4.17. For Gaussian pulse with variance $\sigma = 18$ ns which shows exponential decay when the power of the driving field fall below a certain limit, most power is located around the resonator frequency $\nu_r$. The Gaussian pulse with variance $\sigma = 100$ ns however has almost no power locate at $\nu_r$.

In the previous paragraph we have seen that in our case only the photons in a $6\kappa$ frequency band around the bare resonator frequency contribute to dephasing of the qubit. For a square pulse with the optimal length (pulse ends at a minimum of the transient oscillation), 10% to 40% of the power is located in this band. This could lead to significant dephasing for high powers. Analyzing the Gaussian pulses, the photons in this frequency band can be neglected, which makes them the choice for the ac-Stark pulse, if photon-induced dephasing really turns out to be a problem.

The ideal conditions to perform a measurement of the intra-cavity photon number is a sample with a high Q resonator and high $g^2/\Delta$. While the latter is necessary to reach fast phase gate rates, the first would decrease the photon induced dephasing, since only photons in the small frequency band of $\pm 6\kappa$ around the resonator frequency contribute to dephasing.

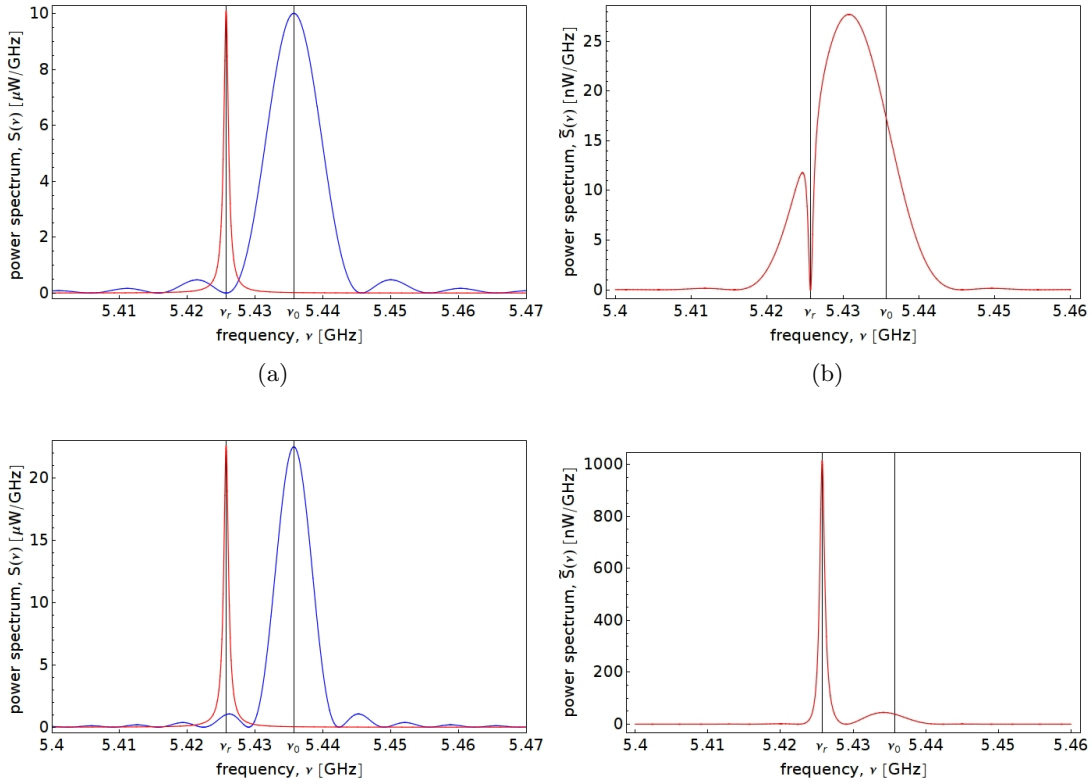


Fig. 4.16: **a)** Power spectrum $S(\nu)$ of a square pulse with a length of 100 ns at a detuning of 10 MHz (blue) and the rescaled Lorentzian curve of the resonator $P(\nu)$ (red). **b)** Power spectrum of the pulse inside the resonator, calculated by multiplying the Lorentzian resonator curve with the power spectrum of the square pulse $\tilde{S}(\nu) = P(\nu)S(\nu)$.**c),d)** Same as in a) and b) but for a square pulse with a length of 150 ns.

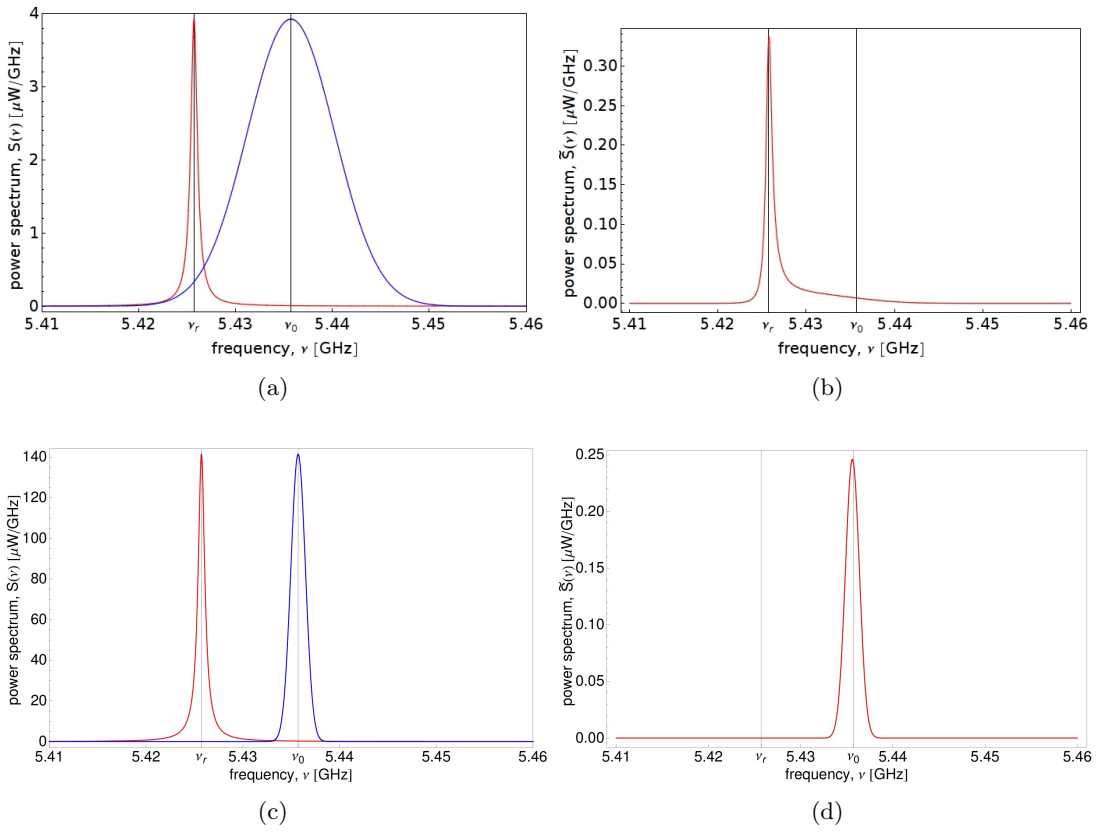


Fig. 4.17: **a)** Power spectrum $S(\nu)$of a Gaussian pulse with a variance of 18 ns at a detuning of 10 MHz (blue) and the rescaled Lorentzian curve of the resonator $P(\nu)$ (red). **b)** Power spectrum of the pulse inside the resonator, calculated by multiplying the Lorentzian resonator curve with the power spectrum of the Gaussian pulse $\tilde{S}(\nu) = P(\nu)S(\nu)$. **c),d)** Same as in a) and b) but for a Gaussian pulse with a variance of 100 ns

# 5 Conclusion

The goal of this diploma thesis was the implementation of a phase gate, which however couldn't be finished. A gate charge instability in our qubit appeared in the middle of the diploma thesis, which made it impossible to perform any measurements on the qubit state. Nevertheless, we have still found some results that are essential to implement the phase gate.

We used as our qubit a superconducting electronic circuit placed inside a microwave resonator. The coupling between intra-cavity photons with the qubit can either be used to measure the qubit state or to realize a phase gate using the ac-Stark effect. Populating the resonator with a certain number of photons with a microwave pulse applied to the resonator accumulates a relative phase in the qubit state in the rotating frame at the qubit transition frequency. This accumulated phase can be measured with a Ramsey type experiment and the average number of photons inside the resonator during the microwave pulse can then be reconstructed. In order to carry out this experiment one has to carefully analyze the response of the cavity due to applied microwave pulses. This has been done for resonant and off resonant microwave pulses with a rectangular and Gaussian envelope function. We have shown, that the response of the resonator to resonant microwave pulses is very slow compared to the dephasing of our qubit state. Off resonant pulses are therefore needed to populate the resonator with photons on a short timescale. Transient oscillations inside the resonator with a frequency of the detuning of the driving field from the resonator frequency turned out to be useful to apply short and well defined microwave pulses. However, this is only true when the pulse ends exactly at a minimum of those transient oscillations, if it ends at a maximum, remaining photons inside the resonator decay exponentially with the slow photon decay rate of the resonator. Analyzing the Gaussian pulses, we have shown that the response of the cavity shows a Gaussian curve only when the variance is higher then a minimal variance $\sigma_{\min}$, which can be lowered significantly by using higher detunings. For variances lower then $\sigma_{\min}$, we observe also a slow exponential decay of intra-cavity photons. We have then analyzed the influence of microwave pulses applied to the resonator on the dephasing of the qubit state. It turned out that for off resonant pulses with rectangular envelope functions, the induced dephasing may be an issue, while off resonant Gaussian pulses with variances higher then $\sigma_{\min}$ don't contribute to dephasing.

Some measurement attempts of the accumulated phase in the qubit state subject to a microwave pulse with the Ramsey type experiment have been carried out. They have

been done however without the exact knowledge of the resonator response to microwave pulses and have therefore not yielded in good results. After the diligent analysis of the microwave pulses presented in this diploma thesis, this shouldn't be much of a problem anymore and is the subject of next measurements.

# 6 Acknowledge

First I would like to kindly thank my supervisor Prof. Dr. Andreas Wallraff for the opportunity to do my diploma thesis in his small research group. He was always here to patiently answer my questions, and never hesitated to share his knowledge in physical aspects. I also want to thank him for correcting and making this report readable. I also would like to thank all my collaborators in the quantum device lab. In particular Romeo Bianchetti, Peter Leek and Johannes Fink who taught me everything about dilution refrigerators, microwave electronics and measurement software as well as several theoretical aspects. I also want to thank Martin Göppel, who worked hard to realize the first charge CPB fabricated at the ETH Zürich, even though it had the same problem as the other sample. It was a pleasure working with you.

# Bibliography


[1] Deutsch, D. Quantum theory, the church-turing principle and the universal quantum computer. *Proceedings of the Royal Society of London. Series A, Mathematical and Physical Sciences* **400**, 97–117 (1985). URL `http://links.jstor.org/sici?sici=0080-4630%2819850708%29400%3A1818%3C97%3AQTTCPA%3E2.0.CO%3B2-A`.

[2] Shor, P. W. Polynomial-time algorithms for prime factorization and discrete logarithms on a quantum computer. *Siam J. Sci. Statist. Comput.* **26**, 1484 (1997). URL `http://www.citebase.org/abstract?id=oai:arXiv.org:quant-ph/9508027`.

[3] Grover, L. K. A fast quantum mechanical algorithm for database search. In *STOC '96: Proceedings of the twenty-eighth annual ACM symposium on Theory of computing*, 212–219 (ACM Press, New York, NY, USA, 1996).

[4] Feynman, R. P. Simulating physics with computers. *International Journal Of Theoretical Physics* **21**, 467–488 (1982).

[5] Wallraff, A. *et al.* Strong coupling of a single photon to a superconducting qubit using circuit quantum electrodynamics. *Nature* **431**, 162–167 (2004).

[6] Schuster, D. I. *et al.* Resolving photon number states in a superconducting circuit. *Nature* **445**, 515–518 (2007).

[7] Cirac, J. I. & Zoller, P. Quantum computations with cold trapped ions. *Physical Review Letters* **74**, 4091–4094 (1995). URL `http://link.aps.org/abstract/PRL/v74/p4091`.

[8] CHUANG, I. L. & YAMAMOTO, Y. Simple quantum computer. *Physical Review A* **52**, 3489–3496 (1995).

[9] Gershenfeld, N. A. & Chuang, I. L. Bulk spin-resonance quantum computation. *Science* **275**, 350–356 (1997).

[10] David G.Cory, A. F. & F.Havel, T. Ensemble quantum computing by nmr spectroscopy. *Proc. Natl. Acad. Sci. USA* **94**, 1624–1639 (1997).

[11] Loss, D. & DiVincenzo, D. P. Quantum computation with quantum dots. *Physical Review A* **57**, 120–126 (1998).

[12] DOMOKOS, P., RAIMOND, J. M., BRUNE, M. & HAROCHE, S. Simple cavity-qed 2-bit universal quantum logic gate - the principle and expected performances. *Physical Review A* **52**, 3554–3559 (1995).

[13] JOSEPHSON, B. D. Possible new effects in superconductive tunnelling. *Physics Letters* **1**, 251–253 (1962).

[14] JAKLEVIC, R. C., SILVER, A. H., LAMBE, J. & MERCEREAU, J. E. Quantum interference effects in josephson tunneling. *Physical Review Letters* **12**, 159–& (1964).

[15] P.Feynman, R. *The Feynman Lectures on Physics*, vol. 3 (Addison-Wesley Publishing Company, 1965).

[16] Büttiker, M. Zero-current persistent potential drop across small-capacitance josephson junctions. *Phys. Rev. B* **36**, 3548–3555 (1987).

[17] Bouchiat, V., Vion, D., Joyez, P., Esteve, D. & Devoret, M. H. Quantum coherence with a single Cooper pair. *Physica Scripta* **T76**, 165–170 (1998).

[18] Nakamura, Y., Pashkin, Y. & Tsai, J. S. Coherent control of macroscopic quantum states in a single-cooper-pair box. *Nature* **398**, 786–788 (1999). URL `http://dx.doi.org/10.1038/19718`.

[19] Vion, D. *et al.* Ramsey fringe measurement of decoherence in a novel superconducting quantum bit based on the cooper pair box. *Physica Scripta* **T102**, 162–166 (2002).

[20] Koch, J. *et al.* Introducing the transmon: a new superconducting qubit from optimizing the cooper pair box. *arXiv:cond-mat/0703002v1* (2007).

[21] Bouchiat, V. *Quantum fluctuations of the charge in single electron and single Cooper pair devices.* Ph.D. thesis, Université Paris VI, CEA-Saclay (1997).

[22] Schuster, D. I. *Circuit Quantum Electrodynamics.* Ph.D. thesis, Yale University (2006).

[23] Cottet, A. *Implementation of a quantum bit in a superconducting circuit.* Ph.D. thesis, Université Paris VI, CEA-Saclay (2002).

[24] Pozar, D. *Microwave Engineering*, vol. 3rd edition (John Wiley & Sons, 2005).

[25] Simons, R. N. Coplanar waveguide circuits, components and systems. *Wiley Series in Microwave and Optical Engineering, Wiley Inter-Science* (2001).

[26] JAYNES, E. T. & CUMMINGS, F. W. Comparison of quantum and semiclassical radiation theories with application to beam maser. *Proceedings Of The Ieee* **51**, 89–& (1963).

[27] C.Gerry, C. & L.Knight, P. *Introductory Quantum Optics* (Cambridge University Press, 2005).

[28] Blais, A., Huang, R. S., Wallraff, A., Girvin, S. M. & Schoelkopf, R. J. Cavity quantum electrodynamics for superconducting electrical circuits: An architecture for quantum computation. *Physical Review A* **69**, 062320 (2004).

[29] Fink, J. M. *Single Qubit Control and Observation of Berry's Phase in a Superconducting Quantum Circuit.* Master's thesis, ETH Zurich (2007).

[30] Breuer, H.-P. & Petruccione, F. *The Theory of Open Quantum Systems* (Oxford University Press, 2007).

[31] Weiss, U. *Quantum Dissipative Systems*, vol. Volume 2 of Series in Modern Condensed Matter Physics (World Scientific Publishing, 1999).

[32] Wallraff, A. *et al.* Approaching unit visibility for control of a superconducting qubit with dispersive readout. *Phys. Rev. Lett.* **95**, 060501 (2005).

[33] Pobell, F. *Matter and methods at low temperatures* (Springer, 1995), 2nd edn.

[34] Schuster, D. I. *et al.* ac stark shift and dephasing of a superconducting qubit strongly coupled to a cavity field. *Physical Review Letters* **94**, 123602 (2005).

[35] Rabi, I. I. Space quantization in a gyrating magnetic field. *Physical Review* **51**, 0652–0654 (1937).

[36] RAMSEY, N. F. A molecular beam resonance method with separated oscillating fields. *Physical Review* **78**, 695–699 (1950).

[37] Gambetta, J. *et al.* Qubit-photon interactions in a cavity: Measurement-induced dephasing and number splitting. *Physical Review A* **74**, 042318 (2006).

[38] C.Gardiner & P.Zoller. *Quantum Noise* (Springer Verlag, 2000).

[39] Abragam, A. *The Principles of Nuclear Magnetism* (Oxford University Press, 2006).

[40] Walls, D. & Milburn, G. *Quantum Optics* (Springer-Verlag, Berlin, 1994).